Journal of Physical Oceanography
September 2019, Volume 49, Pages 2291-2307
https://doi.org/10.1175/JPO-D-19-0061.1
https://archimer.ifremer.fr/doc/00506/61757/

Whitecap and Wind Stress Observations by Microwave Radiometers: Global Coverage and Extreme Conditions

Hwang Paul A. [1,*], Reul Nicolas [2], Meissner Thomas [3], Yueh Simon H. [4]

[1] Remote Sensing Division, U. S. Naval Research Laboratory, Washington, DC 20375 ,USA
[2] Laboratoire d'Océanographie Physique et Spatial (LOPS), Institut Français de Recherche pour l'Exploitation de la Mer (IFREMER), Univ. Brest, CNRS, IRD, Brest, France
[3] Remote Sensing Systems, Santa Rosa, CA 94501, USA
[4] Jet Propulsion Laboratory, California Institute of Technology, Pasadena, CA 91125, USA

* Corresponding author : Paul A. Hwang, email address : paul.hwang@nrl.navy.mil

Abstract :

Whitecaps manifest surface wave breaking that impacts many ocean processes, of which surface wind stress is the driving force. For close to a half century of quantitative whitecap reporting, only a small number of observations are obtained under conditions with wind speed exceeding 25 m/s. Whitecap contribution is a critical component of ocean surface microwave thermal emission. In the forward solution of microwave thermal emission, the input forcing parameter is wind speed, which is used to generate the modeled surface wind stress, surface wave spectrum, and whitecap coverage necessary for the subsequent electromagnetic (EM) computation. In this respect, microwave radiometer data can be used to evaluate various formulations of the drag coefficient, whitecap coverage, and surface wave spectrum. In reverse, whitecap coverage and surface wind stress can be retrieved from microwave radiometer data by employing pre-calculated solutions of an analytical microwave thermal emission model that yields good agreement with field measurements. There are many published microwave radiometer datasets covering a wide range of frequency, incidence angle, and both vertical and horizontal polarizations, with maximum wind speed exceeding 90 m/s. These datasets provide information of whitecap coverage and surface wind stress from global oceans and in extreme wind conditions. Breaking wave energy dissipation rate per unit surface area can be estimated also by making use of its linear relationship with whitecap coverage derived from earlier studies.

1. Introduction

Due to its close connection to wave breaking, there has been an enduring interest in attempting to quantify the ocean surface whitecap coverage. Conventionally, whitecap observations are made with photographs or video recording. The sharp brightness contrast between whitecaps and background water surface is used to determine the fraction of whitecap coverage (e.g., Monahan 1969, 1971; Toba and Chaen 1973; Ross and Cardone 1974; Black et al. 1986; Walker 1994; Xu et al. 2000; Lafon et al. 2004, 2007; Sugihara et al. 2007; Callaghan et al. 2008; Kleiss and Melville, 2011; Holthuijsen et al. 2012; Brumer et al. 2017; and references therein). Over many decades of diligent observations, only a small number of published observations are obtained in conditions with wind speed exceeding about 25 m s^{-1} (e.g., Weather Squadron Two 1952; Black et al. 1986; Holthuijsen et al. 2012). This is mainly caused by the necessity of having a ship or aircraft in the scene to make photographic or video observations, and tower-based operations are suspended during inclement weather.

Microwave radiometer data represent another source of whitecap information. As in ocean surface optical images, microwave brightness temperature T_{bp} increases sharply in the presence of whitecaps (surface foams); subscript p is polarization and is either vertical (V) or horizontal (H) in this paper. Several investigations of whitecap retrieval from T_{bp} data have been reported (e.g., Pandey and Kakar 1982; Wentz 1983; Anguelova and Webster 2006; Hwang 2018; Anguelova and Bettenhausen 2019). Utility of T_{bp}-derived whitecaps for air-sea interaction studies has been demonstrated (Salisbury et al. 2013, 2014; Albert et al. 2016; Anguelova 2016) using WindSat whitecap database built with an earlier version of the $W_c(T_{bp})$ algorithm (Anguelova et al. 2010).

In the present investigation, it is emphasized that the ocean surface microwave thermal emission is composed of two major components: surface roughness and foam. The relative weighting of the two components varies as a function of wind speed, microwave frequency, polarization, and incidence angle.

In general, the roughness term dominates over a wide range of wind speed (Hwang 2012, 2018, 2019). It is therefore very critical to correctly compute the roughness term in order to minimize errors spilled over to the whitecap term.

Both surface roughness and whitecaps are driven by ocean surface wind stress. Forward solutions of microwave thermal emission, with wind speed as the only oceanographic/atmospheric input, require the information of surface wind stress, surface wave spectrum, and whitecap coverage for the EM thermal emission calculation (e.g., Yueh et al. 1994a, b; Johnson and Zhang 1999; Hwang 2012, 2018, 2019). The forward computation procedure therefore employs wind speed dependence models of drag coefficient C_{10}, whitecap coverage W_c, and directional surface wave spectrum $S(\boldsymbol{k})$ reported in literature; $\boldsymbol{k}$ is the wavenumber vector of surface waves (roughness). Good agreement between forward solutions and radiometer data is achieved only when the employed C_{10}, W_c, and $S(\boldsymbol{k})$ models are reasonably accurate. In this respect, microwave radiometer data can be used to evaluate various formulations of the drag coefficient, whitecap coverage, and surface wave spectrum. An example is given in Hwang (2018, Figures 3a and 4) showing that small perturbations of the drag coefficient formula can result in large changes of the thermal emission solution. Similarly, the forward solution of radar backscattering is severely modified by different assumptions of the drag coefficient (Hwang and Fois 2015, Figure 12).

Many reports of microwave radiometer measurements in high winds have been published recently (e.g., Meissner and Wentz 2009; Yueh et al. 2010, 2013, 2016; Klotz and Uhlhorn 2014; Meissner et al. 2014, 2017; Reul et al. 2016; Sapp et al. 2019). These references and datasets are denoted M09, Y10, Y13, Y16, K14, M14, M17, R16, and S19, respectively in this paper. Analyses of these data have led to improved understanding relating surface wind speed with surface wind stress, surface roughness spectrum, and whitecap coverage (Hwang 2012, 2018, 2019). The most recent results are presented in Hwang, Reul, Meissner, and Yueh (2019), which is referred to as HRMY in the remainder of this paper. With improved understanding, good agreement is achieved between analytical thermal emission computations and microwave brightness temperature measurements over a wide range of frequency, incidence angle, both *V* and *H* polarizations, and calm to tropical cyclone (TC) wind conditions (Hwang 2019; HRMY).

Built on this foundation, an algorithm is developed for deriving whitecap coverage and surface wind stress from microwave radiometer measurements. Analytical solutions of wind-induced excess emissivity are pre-calculated to generate lookup tables that serve as geophysical model functions (GMFs). (Emissivity $e_p=T_{bp}/T_s$ is the ratio of brightness temperature T_{bp} and sea surface temperature T_s.) The wind-induced excess emissivity is a relatively small portion of the total emissivity that is dominated by the flat-surface specular term. With the specular term removed, the excess emissivity is more sensitive (compared to T_{bp}) for retrieving wind-related parameters such as whitecap coverage and surface wind stress. Furthermore, analytical thermal emission computation can separate roughness and foam components. By using the foam component, additional improvements are realized in the retrieved results of whitecap coverage and surface wind stress. Microwave data collected in TCs (M09, R16, Y16, M17, and S19) are then processed to yield information of whitecap coverage and surface wind stress in extreme wind conditions.

Section 2 discusses the theoretical aspects of ocean surface microwave thermal emission and the forward computation procedure. The discussion includes a comparison between analytical solutions and field measurements. Section 3 describes the method for retrieving whitecap coverage and surface wind stress using microwave radiometers. Section 4 presents the oceanographic significance of microwave approach and results of retrieved whitecap coverage and surface wind stress from global oceans and in extreme wind conditions. Furthermore, breaking wave energy dissipation rate per unit surface area can be estimated by making use of its linear relationship with whitecap coverage derived from previous studies (Ross and Cardone 1974; Hwang and Sletten 2008). Section 5 is summary.

Accepted for publication in *Journal of Physical Oceanography*. DOI 10.1175/JPO-D-19-0061.1.

2. Ocean surface microwave thermal emission

a. Theoretical background

Sea surface microwave emission is typically given in terms of brightness temperature T_{bp} or emissivity $e_p=T_{bp}/T_s$. In the absence of surface roughness and foam, e_p is dependent on microwave frequency f, incidence angle θ, polarization p, and bulk sea water properties of sea surface temperature T_s and sea surface salinity s. The fundamental property characterizing emissivity is the sea water relative permittivity (dielectric constant) ε (e.g., Klein and Swift 1977; Meissner and Wentz 2004). Knowing ε the Fresnel reflection coefficients of V and H polarizations can be computed:

$$R_{HH}^{(0)}=\frac{\cos\theta-\left(\varepsilon-\sin^2\theta\right)^{1/2}}{\cos\theta+\left(\varepsilon-\sin^2\theta\right)^{1/2}}$$
$$R_{VV}^{(0)}=\frac{\varepsilon\cos\theta-\left(\varepsilon-\sin^2\theta\right)^{1/2}}{\varepsilon\cos\theta+\left(\varepsilon-\sin^2\theta\right)^{1/2}} . \qquad (1)$$

The flat surface (specular) emissivities e_{0V} and e_{0H} are given by:

$$e_{0p}\left(f,\theta\right)=1-\left|R_{pp}^{(0)}\left(f,\theta\right)\right|^2 . \qquad (2)$$

For a foamless flat sea surface, the specular emissivity term is given as

$$e_{0psw}=e_{0p}\left(f,\theta,\varepsilon_{sw}\right)=1-\left|R_{pp}^{(0)}\left(f,\theta,\varepsilon_{sw}\right)\right|^2 , \qquad (3)$$

where ε_{sw} is the (foamless) sea water relative permittivity.

In the presence of wind agitation, wave breaking may entrain air into water and change the ocean surface dielectric property. To quantify foam effects from air in whitecaps, an effective relative permittivity ε_e of air-water mixture is introduced. An extensive discussion of many different formulations of ε_e is given in Anguelova (2008). A concise description is presented in Appendix B of

Accepted for publication in *Journal of Physical Oceanography*. DOI 10.1175/JPO-D-19-0061.1.

HRMY. The present application employs the refractive mixing rule (Birchak et al. 1974; Sihvola and Kong 1988; Sihvola 2000; Anguelova 2008)

$$\varepsilon_e = \left[F_a \varepsilon_a^{1/2} + \left(1 - F_a\right) \varepsilon_{sw}^{1/2} \right]^2, \tag{4}$$

where $\varepsilon_a = 1$ is the relative permittivity of air, ε_{sw} is the relative permittivity of foamless sea water as mentioned earlier, and F_a is the effective air volume fraction. In practice, F_a is connected to the observed whitecap coverage W_c (Hwang 2012, 2019; HRMY), which is an area fraction. So there is an implicit assumption of homogeneous air distribution in the thin surface layer that interacts with EM waves; the microwave skin depth is about 0.002 m at 10 GHz, and 0.01 m at 1.4 GHz (HRMY, Fig. 12).

For a foamed flat sea surface, the specular emissivity term is given as

$$e_{0pf} = e_{0p}\left(f, \theta, \varepsilon_e\right) = 1 - \left| R_{pp}^{(0)}\left(f, \theta, \varepsilon_e\right) \right|^2 . \tag{5}$$

The wind-induced excess emissivity $\Delta e_p = e_p - e_{0p}$ can be separated into foam and roughness components:

$$\Delta e_p = \Delta e_{pf} + \Delta e_{pr} . \tag{6}$$

The foam component Δe_{pf} is defined as the difference between the two specular emissivities of air-entrained (foamed) and foamless sea water surfaces, respectively e_{0pf} and e_{0psw}, i.e.,

$$\begin{aligned} \Delta e_{pf} &= e_{0pf} - e_{0psw} \\ &= e_{0p}\left(f, \theta, \varepsilon_e\right) - e_{0p}\left(f, \theta, \varepsilon_{sw}\right) \\ &= \left| R_{pp}^{(0)}\left(f, \theta, \varepsilon_{sw}\right) \right|^2 - \left| R_{pp}^{(0)}\left(f, \theta, \varepsilon_e\right) \right|^2 \end{aligned} . \tag{7}$$

The roughness component is defined by

$$\Delta e_{pr}\left(f, \theta, \phi\right) = \int_0^\infty \int_0^{2\pi} S\left(k', \phi'\right) g_p\left(f, \theta, \phi, \varepsilon, k', \phi'\right) k' \, d\phi' \, dk', \tag{8}$$

where $S(k, \phi)$ [or $S(\boldsymbol{k})$] is the directional spectrum of surface waves (the ocean surface roughness), k is

Accepted for publication in *Journal of Physical Oceanography*. DOI 10.1175/JPO-D-19-0061.1.

wavenumber, ϕ is azimuth angle referenced to the wind direction, and g_p is the EM weighting function describing the thermal emission contribution of each wavenumber-directional surface wave component; the full expression of g_p is given in Yueh et al. (1994a, b) and Johnson and Zhang (1999). In the original formulation given by Yueh et al. (1994a, b) and Johnson and Zhang (1999), $\varepsilon = \varepsilon_{sw}$ and whitecaps are not explicitly treated. In Hwang (2012, 2018, 2019) and HRMY, $\varepsilon = \varepsilon_e$ is used to compute the roughness term for the more realistic condition with whitecap presence.

The major advance derived from comparing analytical solutions with measurements in a wide range of frequency, incidence angle, and both H and V polarizations is an improved understanding of the dependence on frequency and incidence angle of the foam effects in ocean surface microwave emission. In particular, the effective air fraction F_a can be equated to the whitecap coverage W_c for high EM frequencies (f≥14 GHz) but for lower frequencies F_a is smaller than W_c; more details of the $F_a(W_c)$ function are given in Hwang (2019) and HRMY, and they are not repeated here.

b. Forward computation

In a microwave thermal emission analytical model, the input meteorological parameter is wind speed U_{10}, from which surface wind stress (represented by the wind friction velocity u_* or drag coefficient C_{10}), ocean surface roughness spectrum $S(k, \phi)$, and whitecap coverage W_c are calculated to feed into EM thermal emission computation (section 2a). The F_a needed to evaluate ε_e (4) is calculated from W_c as given by the $F_a(W_c)$ function detailed in HRMY. The whitecap coverage model is determined by comparing microwave emission model results with an extensive dataset (K14) of Stepped Frequency Microwave Radiometer (SFMR) measurements of hurricane reconnaissance and research missions. The comparison analysis (Hwang 2018) confirms the following relationship introduced by Hwang (2012), which is established on the whitecap measurements by Callaghan et al. (2008)

$$W_c = \begin{cases} 0, & u_* \le 0.11\,\text{m/s} \\ 0.30\left(u_* - 0.11\right)^3, & 0.11 < u_* \le 0.40\,\text{m/s} \\ 0.07u_*^{2.5}, & u_* > 0.40\,\text{m/s} \end{cases}. \tag{9}$$

The drag coefficient formula to obtain u_* from U_{10} in TC wind conditions is also determined from comparing microwave emission model results with microwave radiometer data:

$$C_{10} = \begin{cases} 10^{-4}\left(-0.0160U_{10}^2 + 0.967U_{10} + 8.058\right), & U_{10} \le 35\text{m/s} \\ 2.23\times10^{-3}\left(U_{10}/35\right)^{-1}, & U_{10} > 35\text{m/s} \end{cases}. \tag{10}$$

The two matching points of three branches in (9), i.e., u_*=0.11 and 0.40 m s^{-1}, correspond to U_{10}=3.3 and 10.0 m s^{-1}; Hwang (2012, Figure 2) presents Callaghan et al. (2008) data in terms of $W_c(u_*)$ and $W_c(U_{10})$ side by side.

Subsequent analyses show that microwave thermal emission solutions incorporating (9) and (10) are in good agreement with microwave radiometer measurements over a wide range of frequency, incidence angle, and both *V* and *H* polarizations. Datasets used for the additional comparisons include six-frequency SFMR (S19), five-frequency WindSat (M09), and L-band airborne (Y10), Soil Moisture Active Passive (SMAP) (Y13, Y14, M14, Y16, M17), and Soil Moisture and Ocean Salinity (SMOS) (R16), as described in Hwang (2019) and HRMY. It is emphasized that existing direct observations of W_c are restricted to wind speeds lower than about 25 m s^{-1} and although the maximum wind speed of published C_{10} data is much higher, the data scatter is rather large in TC wind conditions. Applicability of (9) and (10) to TC wind conditions is inferred from good agreement between theoretical thermal emission computations and microwave radiometer observations, to be further discussed in section 2c.

The surface wave spectrum model H2018 described in Hwang and Fan (2018) and Hwang (2019) is used to compute the roughness term (8). Independent analyses of H2018 have been performed using active and passive microwave measurements including GMFs of scatterometer L-, C-, and Ku-band backscattering radar cross sections (Wentz et al. 1999; Meissner et al. 2014; Stoffelen et al. 2017),

Accepted for publication in *Journal of Physical Oceanography*. DOI 10.1175/JPO-D-19-0061.1.

WindSat brightness temperature data (M09), and low-pass-filtered mean square slopes (Katzberg and Dunion 2009; Katzberg et al. 2013; Gleason 2013; Gleason et al. 2018) obtained from Global Navigation Satellite System reflectometry (GNSS-R). The details are given in Hwang et al. (2011, 2013), Hwang and Fois (2015), Hwang and Fan (2018), and Hwang (2019).

c. Comparison with field observations

As mentioned in Introduction, several datasets of microwave radiometer measurements in high winds have been published (M09, Y10, Y13, K14, M14, R16, Y16, M17, and S19). These datasets are used to examine various formulations of C_{10} and W_c dependence on U_{10} (Hwang 2012, 2018, 2019; HRMY). Figure 1 summarizes the results from those studies and shows comparison of microwave thermal emission computations and field observations of Δe_p for the datasets mentioned above.

Data from airborne SFMR 6.69 GHz (S19) and spaceborne WindSat five-frequency (M09) measurements are displayed in the top two rows of Figure 1 [Panels (a) - (f)], the two numbers in parentheses at the lower left of each panel are f (in GHz) and θ. For the SFMR normal incidence data (S19) displayed in Panel (a) V and H and identical. The analytical solution (black solid line) is in very good agreement with data except for the maximum wind speed datum (56.9 m s^{-1}), which is suspected of rain contamination; more details are given in Sapp et al. (2019) and Appendix A of HRMY. For WindSat measurements (M09) displayed in Panels (b) – (f), the V and H data and analytical curves are shown with black markers and black lines, respectively; the maximum wind speed is 41.4 m s^{-1}. Again, there is good agreement between analytical solutions and measurements for all frequencies and both polarizations.

The analytical EM model provides solutions of sum, foam, and roughness components, respectively Δe_p, Δe_{pf}, and Δe_{pr}, and they are illustrated with black, cyan, and green curves. For the H polarization, the roughness term (green dashed lines) is greater than the foam term (cyan dashed lines) over a wide range of wind speed. The minimum wind speed that Δe_{pf} exceeds Δe_{pr} is about 22 m s^{-1} for normal incidence (Figure 1a), and greater than 50 m s^{-1} for Earth incidence angle (EIA) θ=~53° (Figures 1b - 1f). The exception to roughness term dominance is for the V polarization of C-band and higher frequencies near 53° EIA where Δe_{Vr} crosses over from positive to negative (Hollinger 1971). The WindSat roughness term Δe_{Vr} (green solid lines in Figures 1b - 1f) is nearly zero or negative, and smaller than the foam term Δe_{Vf} (cyan solid lines).

The bottom row of Figure 1 [Panels (g) - (i)] shows L-band (1.41 GHz) data from SMAP and SMOS satellite missions. Analytical solutions of sum, foam, and roughness components are shown with black-solid, cyan-dashed, and green-dashed-dotted curves. The SMAP data (Y16 and M17, shown with blue and magenta dots respectively) report V (Figure 1g) and H (Figure 1h) polarizations at 40° EIA. The reference wind speed used in Y16 is TC best track information with 90.2 m s^{-1} maximum. The reference wind speed used in M17 is collocated SFMR measurements with 70.9 m s^{-1} maximum. R16 is from five years SMOS measurements of average excess emissivity $\Delta e_A=(\Delta e_V+\Delta e_H)/2$ containing about 300 TC interceptions with continuous EIA coverage between 10° and 65°. Here we consider only a subset of this database corresponding to the SMOS sensor intercepts with Category 4 hurricane Igor developed in North Atlantic in 2010 (Reul et al., 2012). The wind reference is H*WIND analyzed fields (Powell et al., 1998), with 44.3 m s^{-1} maximum wind speed after averaging H*WIND at the spatial resolution of the SMOS instrument (~43 km). Altogether, there are 304602 (U_{10}, Δe_A, θ) triplets. Panel (i) presents the SMAP Δe_A data (Y16 and M17, shown with blue and magenta dots respectively) combined with the SMOS results extracted within 40°±0.1° EIA [2508 (Δe_A, U_{10}) pairs] and given as red contour lines of data density. There is the expected large data scatter of these measurements under TC conditions, and analytical solutions (black lines) provide a good description of their wind speed dependence. The minimum wind speed that Δe_{pf} (cyan curves) exceeds Δe_{pr} (green curves) is about 45 m s^{-1} for Δe_V, 62 m

s^{-1} for Δe_H, and 54 m s^{-1} for Δe_A.

It is gratifying to see that the analytical EM thermal emission model yields solutions in good agreement with a large variety of measurements at different frequencies, incidence angles, and both *V* and *H* polarizations. The capability of the EM thermal emission model to separate roughness and foam components presents an excellent opportunity to explore retrieval of whitecap coverage and its driving force (surface wind stress) from microwave brightness temperature measurements.

3. Whitecaps, surface wind stress, and microwave radiometer signal

The microwave thermal emission analytical solution $\Delta e_p(U_{10})$ in fact depends on many more implicit ocean surface parameters and can be written as $\Delta e_p[U_{10}, W_c, u_*, S(k, \phi), \ldots]$. In this paper, we focus on $\Delta e_p(U_{10}, W_c, u_*)$, which can be pre-calculated for retrieving U_{10} and/or W_c and/or u_* from Δe_p. The pre-calculated solutions can be presented as lookup tables to serve as retrieval GMFs.

The retrieval procedure is illustrated in Figure 2 as an example using the WindSat 6.8 GHz *H* polarization data of about 500 (U_{10}, Δe_H) pairs with 24.8 m s^{-1} maximum wind speed; further discussions of WindSat data are given in section 4a and Appendix A. Figure 2a shows $\Delta e_p(U_{10})$ data with magenta circles and analytical solution with black solid line (polarization *p* is *H* in this example). Using pre-calculated $\Delta e_p(U_{10}, W_c, u_*)$ solutions presented as a lookup table (Table 1), the same data can be presented as $\Delta e_p(W_c)$ and $\Delta e_p(u_*)$ as shown with magenta circles in Figures 2b and 2c, the corresponding analytical model solutions are given by black solid lines. The model solutions can then be used to obtain W_c and u_* from Δe_p; the derived W_c and u_* can be subsequently presented as functions of wind speed. For example, Figure 2d shows the retrieved $W_c(U_{10})$ results with magenta circles, and the red dashed-dotted line is the $W_c(U_{10})$ model curve (9).

The analytical thermal emission computation can separate roughness and foam components: Δe_{pr} and Δe_{pf}, respectively. Using the foam component, i.e., employing $\Delta e_{pf}(W_c)$ and $\Delta e_{pf}(u_*)$, can improve the

Accepted for publication in *Journal of Physical Oceanography*. DOI 10.1175/JPO-D-19-0061.1.

results of retrieved whitecap and surface wind stress. The "observed" foam component Δe_{pf} is calculated from observed Δe_p multiplied with the analytical ratio $\Delta e_{pf}/\Delta e_p$ (interpolated to wind speeds of observed Δe_p data). In Figures 2a-2c, the "observed" Δe_{pf} are shown with cyan pluses, and the corresponding model solutions $\Delta e_{pf}(U_{10})$, $\Delta e_{pf}(W_c)$, and $\Delta e_{pf}(u_*)$ are given by blue dashed lines. Retrieving W_c or u_* from Δe_{pf} employs the same procedure outlined in the last paragraph for retrieving W_c or u_* from Δe_p, The results of $W_c(U_{10})$ obtained with Δe_{pf} are given with cyan pluses in Figure 2d, showing less data scatter and in better agreement with the model curve (red dashed-dotted line) in comparison with those derived from Δe_p (magenta circles). Figures 2e and 2f compare modeled and retrieved W_c and u_* using Δe_p (magenta circles) and Δe_{pf} (cyan pluses), again showing less data scatter and better accuracy in the results derived from Δe_{pf} compared to those obtained from Δe_p. The statistics of bias, slope of linear regression, root mean square (RMS) difference, and correlation coefficient (b_0¸ b_1¸ b_2¸ and b_3, respectively) of comparing modeled and retrieved W_c (in percent) and u_* (in m s^{-1}) from Δe_{pf} and Δe_p are printed above Figures 2e and 2f.

4. Result and discussion

a. Global coverage

Spaceborne microwave radiometers provide global coverage. Here we use WindSat data to demonstrate the retrieval of global whitecap coverage and surface wind stress. WindSat is a satellite-based polarimetric microwave radiometer developed by the U. S. Naval Research Laboratory (NRL) Remote Sensing Division and Naval Center for Space Technology for U.S. Navy and National Polar-orbiting Operational Environmental Satellite System (NPOESS) Integrated Program Office (IPO). It was launched in January 2003 to demonstrate the ability to measure ocean surface vector winds with microwave radiometers from space. In addition to surface wind vector, WindSat also measures sea

Accepted for publication in *Journal of Physical Oceanography*. DOI 10.1175/JPO-D-19-0061.1.

surface temperature, columnar atmospheric water vapor, and columnar atmospheric cloud liquid water (Gaiser et al. 2004; Bettenhausen et al. 2006).

Figures 3 and 4 give examples of retrieved whitecap coverage and surface wind stress over a period of about 10.2 h each in northern and southern winters, respectively on 05 Jan 2014 and 01 Jul 2014 with maximum wind speeds 29.5 and 27.9 m s^{-1}. The retrieval lookup tables are given in the supplemental material. Panels (a) and (b) show spatial patterns of W_c and u_* obtained from 10.7 GHz Δe_H, Panels (c) and (d) show $W_c(U_{10})$ and $u_*(U_{10})$ obtained from 10.7, 18.7, 23.8, and 37.0 GHz Δe_H, and their comparison with the $W_c(U_{10})$ and $u_*(U_{10})$ models illustrated with black dashed lines, i.e., (9) and (10), respectively. Results derived from each frequency are averaged into 20 wind speed bins. Consistent W_c and u_* retrievals are obtained from different microwave frequencies. To get an assessment of data scatter, un-averaged 10.7 GHz results are displayed with cyan dots in Panels c and d.

M09 represents WindSat T_{bp} measurements for years 2003 and 2004 and it includes much higher wind speed data (to about 41.4 m s^{-1} maximum) in comparison to those ~10 h snapshots shown in Figures 3 and 4. M09 uses National Centers for Environmental Prediction (NCEP) General Data Assimilation System (GDAS) wind vectors and Special Sensor Microwave Imager (SSM/I) atmospheres for training and testing of a wind-speed retrieval algorithm that can be applied globally and under all existing rain conditions and low wind speeds. H*WIND analyzed wind fields from 17 hurricanes during 2003 and 2004 are used for training and testing the wind vector retrieval algorithm under TC conditions. Retrieved whitecap and surface wind stress results using M09 WindSat data are shown in Figure 5, they are in very good agreement with the $W_c(U_{10})$ and $u_*(U_{10})$ models [(9) and (10)] illustrated with black dashed lines. The global coverage of satellite operation offers an opportunity to obtain measurements in high wind regions that are dangerous, expensive, and difficult to deploy ships or aircraft. More details on WindSat data analysis are given in Appendix A.

Accepted for publication in *Journal of Physical Oceanography*. DOI 10.1175/JPO-D-19-0061.1.

b. Extreme conditions

As mentioned earlier, there are several published microwave radiometer datasets dedicated to TC extreme wind conditions. In particular, the maximum winds of Y16 and M17 are 90.2 and 70.9 m s^{-1}, respectively. Both Y16 and M17 report SMAP radiometer data; the Y16 reference wind is TC best track maximum winds in both Pacific and Atlantic Oceans, whereas the M17 reference wind is collocated SFMR data. Figures 6a and 6b show retrieved W_c and u_* from these two datasets using Δe_{pf} of both V and H polarizations; the retrieval lookup tables are given in the supplemental material. Statistics (b_0, b_1, b_2, and b_3) of comparing $W_c(U_{10})$ and $u_*(U_{10})$ models with microwave-retrieved results for both datasets are printed at the lower-right corners. Slightly higher RMS difference (b_2) and less-linear regression slope (b_1) are found in Y16 compared to those in M17, most likely indicating a better quality of the reference SFMR winds used in M17 compared to the TC best track maximum winds used in Y16. The correlation coefficients (b_3) are all better than 0.91 even for these extreme wind datasets.

Another dataset of great interest is R16 SMOS Δe_A measurements, which have continuous θ coverage from 10° to 65°. Figure 7 shows retrieved W_c and u_* using Δe_{Af} with EIA in the ranges of 11°±0.25°, 15°±0.25°, 20°±0.25°, …, 60°±0.25°, and 64°±0.25°; consistent W_c and u_* retrievals are obtained and they are in good agreement with $W_c(U_{10})$ and $u_*(U_{10})$ models shown with dashed lines. To get an assessment of data scatter, un-averaged 35°±0.25° results are shown in the background with cyan dots.

c. Wave breaking inference

One of the primary reasons for studying whitecap coverage is to infer wave breaking properties. For example, a linear relationship between whitecap coverage W_c and wave breaking energy dissipate rate per unit surface area E_t has been proposed by Ross and Cardone (1974) and Hwang and Sletten (2008). Figure 8 reproduces partially Figure 6 of Hwang and Sletten (2008), showing W_c dependence on U_{10} and E_t. The whitecap observations described in Hwang and Sletten (2008) are collectively referred to as

MTRXLS (Monahan 1971; Toba and Chaen 1973; Ross and Cardone 1974; Xu et al. 2000; Lafon et al. 2004, 2007; Sugihara et al. 2007) and plotted with green dots in Figure 8a. Here, whitecap observations by Callaghan et al. (2008) are also added (labeled C08 and plotted with magenta diamonds in Figure 8a). E_t can be calculated for the four references reporting significant wave height H_s and dominant wave period T_p in addition to U_{10} (Toba and Chaen 1973; Lafon et al. 2004, 2007; Sugihara et al. 2007); these data are displayed with green circles and labeled TLS in the figure. Bin-averaged E_t results are given by black circles in Figure 8b and they can be approximated by the linear $W_c(E_t)$ function given by Hwang and Sletten (2008):

$$W_c = 0.014\left(E_t - 0.014\right), \tag{11}$$

where the unit of E_t is W m^{-2}. Plotted in log-log scales in Figure 8b, the linear function (11) deviates from a straight line when E_t is small. Log-log scales are used because the data ranges of W_c and E_t stretch 2 to 5 orders of magnitude.

The monotonically increasing trend of microwave excess emissivity with wind speed (Figure 1) is a strong indication that surface wind stress and whitecap coverage also increase monotonically with wind speed. In TC wind fields (U_{10}>~35 m s^{-1}) the drag coefficient model (10), with $C_{10} \propto U_{10}^{-1}$, specifies that wind stress (proportional to $u_*^2 = C_{10}U_{10}^2$) increases linearly with wind speed; and whitecap coverage (9) increases slightly stronger than linear with wind speed (~$U_{10}^{1.25}$) and reaches 100% at ~108 m s^{-1}. Combining all the microwave radiometers discussed in this paper (SFMR, SMAP, SMOS, and WindSat), the retrieved whitecap and surface wind stress results are given in Figures 9a and 9b. Applying the $E_t(W_c)$ linear dependence (11), $E_t(U_{10})$ is given in Figure 9c.

d. Remote sensing and ocean surface processes

Ocean remote sensing is interdisciplinary and requires coherent consideration from both remote

Accepted for publication in *Journal of Physical Oceanography*. DOI 10.1175/JPO-D-19-0061.1.

sensing and oceanographic perspectives. In general, our understanding of the relevant oceanographic processes lags behind EM theories. Pertaining to forward computation in support of remote sensing of the ocean environment, particularly winds and waves, the three most relevant oceanographic parameters are the ocean surface roughness (wave) spectrum, whitecaps from wave breaking, and their driving force: surface wind stress. In this paper, we present a holistic approach incorporating all three oceanographic parameters in the analysis.

The approach is two-way. In forward computations, active and passive microwave remote sensing measurements are used to improve our models of C_{10}, W_c, and $S(\boldsymbol{k})$ as functions of wind speed U_{10}. In reverse, the improved ocean modules [C_{10}, W_c, and $S(\boldsymbol{k})$] provide feedback to improve and enhance the remote sensing effort to derive ocean parameters from microwave measurements.

In addition to wind velocity currently retrieved operationally, our analysis shows that the forward solutions of microwave radiometer thermal emission can serve as the GMFs for retrieving additional ocean surface properties, particularly surface wind stress and whitecap coverage, from microwave radiometer measurements. Furthermore, information such as wave breaking energy dissipate rate per unit surface area can be inferred.

5. Summary

The microwave radiometer signal from ocean surface is composed of two major components: roughness (surface waves) and foam (whitecaps). Both ocean surface roughness and whitecaps are driven by ocean surface wind stress, which is connected to wind speed by a drag coefficient. An extensive collection of microwave radiometer data provides the opportunity to critically examine various wind speed functions of drag coefficient and whitecap coverage by comparing microwave thermal emission model results with microwave radiometer measurements in a wide range of microwave frequency (1.4 to 37.0 GHz), incidence angle (0° to 65°), both horizontal and vertical polarizations, and

Accepted for publication in *Journal of Physical Oceanography*. DOI 10.1175/JPO-D-19-0061.1.

an expansive wind speed range covering calm to TC wind conditions. These analyses have shown that the whitecap and drag coefficient models (9) and (10) yield very good agreement between analytical microwave thermal emission computations and all the high-wind microwave radiometer measurements we have assembled, as summarized concisely in Figure 1. The analytical thermal emission model quantifies the relative importance of roughness and foam contributions. In general the roughness term dominates over a wide wind speed range. Retrieving whitecap information using microwave radiometer measurements and based on analytical thermal emission models requires an accurate accounting of the surface roughness contribution.

With a microwave thermal emission model, $\Delta e_p(U_{10}, W_c, u_*)$ and $\Delta e_{pf}(U_{10}, W_c, u_*)$ analytical solutions can be pre-calculated and presented as lookup tables to serve as GMFs for retrieving W_c and u_* from Δe_p and Δe_{pf}. Whitecap coverage and surface wind stress data derived from microwave radiometer measurements in extreme wind conditions and global oceans are presented in this paper and compared to models (9) and (10). In addition, breaking wave energy dissipation rate per unit surface area can be estimated by making use of its linear relationship with whitecap coverage (11) established from previous studies (Ross and Cardone 1974; Hwang and Sletten 2008). Based on the whitecap and surface wind stress models (9) and (10), under TC wind conditions (U_{10}>~35 m s^{-1}) surface wind stress increases with wind speed linearly, whitecap coverage increases with wind speed slightly stronger than linear (~$U_{10}^{1.25}$) and reaches 100% at ~108 m s^{-1}. Given the linear relationship between E_t and W_c, the E_t dependence on wind speed is expected to follow the same trend of whitecaps (Figure 9).

Appendix A. Additional information on the WindSat analysis

For Figures 3 and 4 in this study, we have used four high-frequency (10.7, 18.7, 23.8, and 37.0 GHz) WindSat data in Jan and Jul 2014, which are in northern and southern winters respectively. The 6.8 GHz data are only available at a lower resolution (50 km by 71 km) compared to the four higher frequencies

Accepted for publication in *Journal of Physical Oceanography*. DOI 10.1175/JPO-D-19-0061.1.

(25 km by 35 km). The 6.8 GHz data are used in Figure 2 to serve as a retrieval example.

Data extracted from WindSat Sensor Data Record (SDR) and Environmental Data Record (EDR) include *V* and *H* brightness temperatures (T_V and T_H), EIAs (θ), sea surface temperature (T_s), wind speed (U_{10}), and measurement location (latitude and longitude). The brightness temperature received at sensor antenna is processed to obtain the brightness temperature at sea surface by correcting for atmospheric emissions and cosmic microwave background radiation (Anguelova and Bettenhausen 2019). Rain-flagged data are excluded in this analysis.

The information of wind-related processes (whitecaps and surface wind stress in this study) is contained in the excess emissivity, which is a small fraction of the total surface emissivity $e_p=T_{bp}/T_s$. The flat surface (specular) emissivity is estimated by the portion of data with U_{10}<2 m s^{-1} (Figure A1, measurements are shown with dots of different colors for different frequencies), which can be approximated by polynomial functions of T_s (black curves in the figure). These empirical e_{0p} functions differ slightly for different datasets (the top row in Figure A1 represents 05 Jan 2014 data shown in Figure 3, and the bottom row represents 01 Jul 2014 data shown in Figure 4). The coefficients of polynomial functions are listed in Table B1. The empirical e_{0p} functions deviate from analytical solutions computed with single values of sea surface salinity and sea surface temperature (35 psu and 290 K are used and shown with red lines in the figure); the difference also reflects imperfection of corrections applied to obtaining the brightness temperature at sea surface from the brightness temperature received at antenna.

Figure A2 shows excess emissivity Δe_p for the same period in Figure 3; results for the same period in Figure 4 are similar. Un-averaged data are displayed in the background with light colored dots (cyan for *H* and green for *V*) and bin-averaged results are given with blue markers (squares for *H* and triangles for *V*). They are in very good agreement with those reported in M09, which are superimposed in the figure with red markers (diamonds for *H* and triangles for *V*). Analytical solutions are in excellent agreement with measurements for the *H* polarization (dashed lines) and slightly underestimate the *V* polarization (solid lines) in the wind speed range between about 10 and 30 m s^{-1} (but within about 0.01 Δe_V magnitude).

For θ in the range between 50° and 55°, the Δe_V dependence on wind speed is relatively mild in low to moderate wind speeds. The analytical solutions are in fact nonmonotonic for 18.7, 23.8, and 37.0 GHz. The nonmonotonic trend is also found in the M09 dataset: the lowest wind speed (11.6 m s^{-1}) M09 37.0 GHz datum is negative; also, see Figure 8 in Meissner and Wentz (2012). The lack of wind sensitivity makes it unsuitable to use WindSat Δe_V measured in the neighborhood of 50° to 55° EIA for retrieving whitecap and wind stress (as well as wind speed) except in very high winds. WindSat results of whitecap and wind stress retrieval presented in this paper are based on Δe_H. As a related note, for L band (~1.4 GHz) the critical incidence angle of wind insensitivity moves up to about 70°; see e.g., Yueh et al. (2010) and Hwang (2012, 2019). Whitecap coverage and surface wind stress can be retrieved from the full EIA range of R16 SMOS dataset (Figure 7).

Acknowledgements

This work is sponsored by the Office of Naval Research (Funding Doc. No. N0001416WX00044). We are grateful for the comments and suggestions from two anonymous reviewers. M. Anguelova, M. Bettenhausen, and P. Gaiser kindly provided the WindSat Jan and Jul 2014 data, and the related discussions. Other datasets used in this analysis are given in the references cited. The processing codes and data segments are also available by contacting the corresponding author. NRL Publication Number JA/7260—19-0353.

References

Albert, M. F. M. A., M. D. Anguelova, A. M. M. Manders, M. Schaap, and G. de Leeuw, 2016: Parameterization of oceanic whitecap fraction based on satellite observations. *Atmos. Chem. Phys.*, **16**, 13725–13751. https://doi.org/10.5194/acp-16-13725-2016.

Anguelova, M. D., 2008: Complex dielectric constant of sea foam at microwave frequencies. *J. Geophys. Res.*, **113**, C08001, 1-22, doi:10.1002/2007JC004212.

Anguelova, M. D., 2016: Assessing the utility of satellite-based whitecap fraction to estimate sea spray production and CO2 transfer velocity. *IOP Conf. Ser.: Earth Environ. Sci*., **35**, 012002. https://doi.org/10.1088/1755-1315/35/1/012002.

Anguelova, M. D., and M. H. Bettenhausen, 2019: Whitecap fraction from satellite measurements: Algorithm description. *J. Geophys. Res.*, **124**, 1827-1857, doi: 10.1029/2018JC014630.

Anguelova, M. D., and F. Webster, 2006: Whitecap coverage from satellite measurements: A first step toward modeling the variability of oceanic whitecaps. *J. Geophys. Res*., **111**, C03017. https://doi.org/10.1029/2005JC003158

Anguelova, M. D., M H. Bettenhausen, W. F. Johnston, and P. W. Gaiser, 2010: First extensive whitecap database and its use to study whitecap fraction variability. Paper presented at *17th Air-Sea Interaction Conf.*, Am. Meteorol. Soc., Annapolis, MD. https://ams.confex.com/ams/pdfpapers/174036.pdf

Bettenhausen, M. H., C. K. Smith, R. M. Bevilacqua, N.-Y. Wang, P. W. Gaiser, and S. Cox, 2006: A nonlinear optimization algorithm for WindSat wind vector retrievals. *IEEE Trans. Geosci. Remote Sens.*, **44**, 597–610.

Birchak, J. R., L. G. Gardner, J. W. Hipp, and J. M. Victor, 1974: High dielectric constant microwave probes for sensing soil moisture. *Proc. IEEE*, **62**, 93–98.

Black, P., R. W. Burpee, N. M. Dorst, and W. L. Adams, 1986: Appearance of the sea surface in tropical cyclones. *Weather and Forecasting*, **1**, 102-107,

Brumer, S. E., C. J. Zappa, I. M. Brooks, H. Tamura, S. M. Brown, B. W. Blomquist, C. W. Fairall, and A. Cifuentes-Lorenzen, 2017: Whitecap coverage dependence on wind and wave statistics as observed during SO GasEx and HiWinGS. *J. Phys. Oceanogr.*, **47**, 2211-2235.

Callaghan, A. H., G. de Leeuw, L. H. Cohen, and C. D. O’Dowd, 2008: The relationship of oceanic whitecap coverage to wind speed and wind history. *Geophys. Res. Lett.*, **35**, L23609, doi:10.1029/2008GL036165.

Gaiser, P. W., K. M. St. Germain, E. M. Twarog, G. A. Poe, W. Purdy, D. Richardson, W. Grossman, W. L. Jones, D. Spencer, G. Golba, J. Cleveland, L. Choy, R. M. Bevilacqua, and P. S. Chang, 2004: The WindSat spaceborne polarimetric microwave radiometer: Sensor description and early orbit performance. *IEEE Trans. Geosci. Remote Sens.*, **42**, 2347–2361.

Hollinger, J. P. 1971: Passive microwave measurements of sea surface roughness. *IEEE Trans. Geosci. Electron.,* **9**, 165-169.

Holthuijsen, L. H., M. D. Powell, and J. D. Pietrzak, 2012: Wind and waves in extreme hurricanes. *J. Geophys. Res.*, **117**, C09003.

Hwang, P. A., 2012: Foam and roughness effects on passive microwave remote sensing of the ocean. *IEEE Trans. Geos. Rem. Sens*., **50**, doi: 10.1109/TGRS.2011.2177666, 2978-2985.

Hwang, P. A., 2018: High wind drag coefficient and whitecap coverage derived from microwave radiometer observations in tropical cyclones. *J. Phys. Oceanogr.*, **48**, 2221-2232, doi: 10.1175/JPO-D-18-0107.1.

Hwang, P. A., 2019: Surface foam and L-band microwave radiometer measurements in high winds. *IEEE Trans. Geos. Rem. Sens.*, **57**, 2766-2776, doi: 10.1109/TGRS.2018.2876972.

Accepted for publication in *Journal of Physical Oceanography*. DOI 10.1175/JPO-D-19-0061.1.

Hwang, P. A., and Y. Fan, 2018: Low-frequency mean square slopes and dominant wave spectral properties: Toward tropical cyclone remote sensing. *IEEE Trans. Geos. Rem. Sens.*, **56**, 7359-7368, doi: 10.1109/TGRS.2018.2850969.

Hwang, P. A., and F. Fois, 2015: Surface roughness and breaking wave properties retrieved from polarimetric microwave radar backscattering. *J. Geophys. Res*., **120**, 3640-3657, doi:10.1029/2015JC010782.

Hwang, P. A., and M. A. Sletten, 2008: Energy dissipation of wind-generated waves and whitecap coverage. *J. Geophys. Res*., **113**, C02012, 1-12, doi:10.1029/2007JC004277 (Corrigendum, **114**, C02015, doi:10.1029/2008JC005244, 2009).

Hwang, P. A., D. M. Burrage, D. W. Wang, and J. C. Wesson, 2011: An advanced roughness spectrum for computing microwave L-Band emissivity in sea surface salinity retrieval. *IEEE Geos. Rem. Sens. Lett*., **8**, 547-551, doi: 10.1109/LGRS.2010.2091393.

Hwang, P. A., D. M. Burrage, D. W. Wang, and J. C. Wesson, 2013: Ocean surface roughness spectrum in high wind condition for microwave backscatter and emission computations. *J. Atmos. Oceanic Tech.*, **30**, 2168-2188, doi: 10.1175/JTECH-D-12-00239.1.

Hwang, P. A., N. Reul, T. Meissner, and S. H. Yueh, 2019: Ocean surface foam and microwave emission: Dependence on frequency and incidence angle. *IEEE Trans. Geos. Rem. Sens.* (in press).

Johnson, J. T., and M. Zhang, 1999: Theoretical study of the small slope approximation for ocean polarimetric thermal emission. *IEEE Trans. Geosci. Remote Sens.*, **37**, 2305-2316.

Klein, L. A., and C. T. Swift, 1977: An improved model for the dielectric constant of sea water at microwave frequencies. *IEEE Trans. Antennas Propag.*, **25**, 104-111.

Kleiss, J. M., and W. K. Melville, 2011: The analysis of sea surface imagery for whitecap kinematics. *J. Atmos. Oceanic Technol.*, **28**, 219-243.

Klotz, B. W., and E. W. Uhlhorn, 2014: Improved Stepped Frequency Microwave Radiometer tropical cyclone surface winds in heavy precipitation. *J. Atmos. Oceanic Technol.*, **31**, 2392–2408, doi:10.1175/JTECH-D-14-00028.1.

Lafon, C., J. Piazzola, P. Forget, O. Le Calve, and S. Despiau, 2004: Analysis of the variations of the whitecap fraction as measured in a coastal zone. *Bound.-Layer Meteorol.*, **111**, 339-360.

Lafon, C., J. Piazzola, P. Forget, and S. Despiau, 2007: Whitecap coverage in coastal environment for steady and unsteady wave field conditions. *J. Mar. Syst.*, **66**, 38-46.

Meissner, T. and F. J. Wentz, 2004: The complex dielectric constant of pure and sea water from microwave satellite observations. *IEEE Trans. Geosci. Rem. Sens.*, **42**, 1836-1849.

Meissner, T. and F. J. Wentz, 2009: Wind-vector retrievals under rain with passive satellite microwave radiometers. *IEEE Trans. Geosci. Rem. Sens.*, **47**, 3065-3083.

Meissner, T., and F. J. Wentz, 2012: The emissivity of the ocean surface between 6 and 90 GHz over a large range of wind speeds and earth incidence angles. *Trans. Geosci. Remote Sens*., **50**, 3004-3026. doi:10.1109/TGRS.2011.2179662

Meissner, T., L. Ricciardulli, and F. Wentz, 2014: The emission and scattering of L-band microwave radiation from rough ocean surfaces and wind speed measurements from the Aquarius sensor. *J. Geophys. Res. Oceans*, **119**, 6499–6522, doi:10.1002/2014JC009837.

Meissner, T., L. Ricciardulli, and F. Wentz, 2017: Capability of the SMAP mission to measure ocean surface winds in storms. *Bull. Am. Meteorol. Soc.*, **98**, 1660-1677.

Monahan, E. C., 1969: Fresh water whitecaps. *J. Atmos. Sci.*, **26**, 1026-1029.

Monahan, E. C., 1971: Oceanic whitecaps, *J. Phys. Oceanogr*., **1**, 139-144.

Pandey, P., and R. Kakar, 1982: An empirical microwave emissivity model for a foam-covered sea. *J. Oceanic Eng.*, **7**, 135– 140. doi:10.1109/JOE.1982.1145527.

Powell, M. D., S. H. Houston, L. R. Amat, and N. Morisseau-Leroy, 1998: The HRD real-time hurricane wind analysis system. *J. Wind Eng. Ind. Aerodyn*., **77–78**, 53–64, doi:10.1016/S0167-

Accepted for publication in *Journal of Physical Oceanography*. DOI 10.1175/JPO-D-19-0061.1.

6105(98)00131-7.

Reul, N., J. Tenerelli, B. Chapron, D. Vandemark, Y. Quilfen, and Y. Kerr, 2012: SMOS satellite L-band radiometer: A new capability for ocean surface remote sensing in hurricanes. *J. Geophys. Res.*, **117**, C02006, doi:10.1029/2011JC007474.

Reul, N., B. Chapron, E. Zabolotskikh, C. Donlon, Y. Quilfen, S. Guimbard, and J. F. Piolle, 2016: A revised L-band radio-brightness sensitivity to extreme winds under tropical cyclones: The five year SMOS-storm database. *Remote Sens. Environ.*, **180**, 274–291, doi:10.1016/j.rse.2016.03.011.

Ross, D. B., and V. Cardone, 1974: Observations of oceanic whitecaps and their relation to remote measurements of surface wind stress. *J. Geophys. Res.*, **79**, 444-452.

Salisbury, D. J., M. D. Anguelova, and I. M. Brooks, 2013: On the variability of whitecap fraction using satellite-based observations. *J. Geophys. Res.*, **118**, 6201–6222. https://doi.org/10.1002/2013JC008797.

Salisbury, D. J., M. D. Anguelova, and I. M. Brooks, 2014: Global distribution and seasonal dependence of satellite-based whitecap fraction. *Geophys. Res. Lett.*, **41**, 1616–1623. https://doi.org/10.1002/2014GL059246.

Sapp, J. W., S. O. Alsweiss, A. Jelenak, P. S. Chang, and J. Carswell, 2019: Stepped frequency microwave radiometer wind-speed retrieval improvements. *Rem. Sens.*, **11**, 214(1-25), doi:10.3390/rs11030214.

Sihvola, A. H., 2000: Mixing rules with complex dielectric coefficients. *Subsurf. Sens. Tech. Appl.*, **1**, 393-415.

Sihvola, A. H., and J. A. Kong, 1988: Effective permittivity of dielectric mixtures. *IEEE Trans. Geosci. Remote Sens.*, **26**, 420–429.

Stoffelen, A. J. Adriaan, V. Verspeek, J. Vogelzang, and A. Verhoef, 2017: The CMOD7 geophysical model function for ASCAT and ERS wind retrievals. *IEEE J. Sel. Topics Appl. Earth Obs. Remote*

Sens., **10**, 2023-2134.

Sugihara, Y., H. Tsumori, T. Ohga, H. Yoshioka, and S. Serizawa, 2007: Variation of whitecap coverage with wave-field conditions. *J. Mar. Syst.*, **66**, 47-60.

Toba, Y., and M. Chaen, 1973: Quantitative expression of the breaking of wind waves on the sea surface. *Records Oceanogr. Works Japan*, **12**, 1-11.

Walker, R. E., 1994: *Marine Light Field Statistics*. John Wiley, Hoboken, N.J., 675 pp.

Weather Squadron Two, 1952: Wind Estimations from aerial observations of sea conditions. NAS Jacksonville, http://www.aoml.noaa.gov/hrd/hurdat/seastate-aircraft.pdf.

Wentz, F. J., 1983: A model function for ocean microwave brightness temperatures. *J. Geophys. Res.*, **88**, 1892–1908. doi:10.1029/JC088iC03p01892.

Wentz, F. J., and D. K. Smith, 1999: A model function for the ocean-normalized radar cross section at 14 GHz derived from NSCAT observations. *J. Geophys. Res.*, **104**, 11499-11514.

Xu, D., X. Liu, and D. Yu, 2000: Probability of wave breaking and whitecap coverage in a fetch-limited sea. *J. Geophys. Res.*, **105**, 14253-14259.

Yueh, S.H., R. Kwok, F.K. Li, S.V. Nghiem, W.J. Wilson, and J.A. Kong, 1994a: Polarimetric passive remote sensing of ocean wind vectors. *Radio Sci.*, **29**, 799-814.

Yueh, S. H., R. Kwok, and S. V. Nghiem, 1994b: Polarimetric scattering and emission properties of targets with reflection symmetry. *Radio Sci.*, **29**, 1409-1420.

Yueh, S. H., S. J. Dinardo, A. G. Fore, and F. K. Li, 2010: Passive and active L-band microwave observations and modeling of ocean surface winds. *IEEE Trans. Geos. Rem. Sens.*, **48**, 3087-3100.

Yueh, S. H., W. Tang, A. G. Fore, G. Neumann, A. Hayashi, A. Freedman, J. Chaubell, and G. S. E. Lagerloef, 2013: L-band passive and active microwave geophysical model functions of ocean surface winds and applications to Aquarius retrieval. *IEEE Trans. Geos. Remote Sens.*, **51**, 9, 4619-4632.

Yueh, S. H., A. G. Fore, W. Tang, A. Hayashi, B. Stiles, N. Reul, Y. Weng, and F. Zhang, 2016: SMAP

L-band passive microwave observations of ocean surface wind during severe storms. *IEEE Trans. Geos. Remote Sens.*, **54**, 12, 7339-7350.

Accepted for publication in *Journal of Physical Oceanography*. DOI 10.1175/JPO-D-19-0061.1.

List of Figures

Figure 1. Calculated Δe_V and Δe_H at various microwave frequencies, and comparison with field data. Top two rows (M09 and S19, triangle for *V* and square for *H*): (a) 6.69 GHz, (b) 6.8 GHz, (c) 10.7 GHz, (d) 18.7 GHz, (e) 23.8 GHz, and (f) 37.0 GHz. Sum, foam and roughness contributions are given by black, cyan and green curves, solid and dashed lines show vertical and horizontal polarizations, respectively. The two numbers in parentheses are frequency (in GHz) and EIA. Bottom row (L band 1.41 GHz, θ=40°): (g) Δe_V, Y16 and M17 (SMAP), (h) Δe_H, Y16 and M17 (SMAP), and (i) Δe_A, Y16 and M17 (SMAP) and R16 θ=40°±0.1° (SMOS).

Figure 2. Illustration of whitecap and surface wind stress retrieval using Δe_p, WindSat 6.8 GHz horizontal polarization data are used for example (p =H): (a) $\Delta e_p(U_{10})$ and $\Delta e_{pf}(U_{10})$, (b) $\Delta e_p(W_c)$ and $\Delta e_{pf}(Wc)$, (c) $\Delta e_p(u_*)$ and $\Delta e_{pf}(u_*)$, (d) $W_c(U_{10})$ retrieved with Δe_p and Δe_{pf}, (e) comparison of modeled and retrieved W_c from Δe_p and Δe_{pf}, and (f) comparison of modeled and retrieved u_* from Δe_p and Δe_{pf}. In (e) and (f), statistics (b_0, b_1, b_2, and b_3) of modeled and retrieved W_c and u_* with Δe_p and Δe_{pf} are printed at the top.

Figure 3. Snapshots (~10 h) of WindSat global retrieval of (a) W_c, and (b) u_* on 05 Jan 2014 (in northern winter). The dependence on wind speed is given in (c) for W_c, and (d) for u_*, bin-averaged results shown with colored markers are from four microwave frequencies identified in the legend; un-averaged results for 10.7 GHz are superimposed with cyan dots in the background.

Figure 4. As Figure 3 but on 01 Jul 2014 (in southern winter).

Figure 5. Whitecap and wind stress retrieval from five frequencies of M09 WindSat dataset and comparison with models (9) and (10): (a) W_c, and (b) u_*.

Accepted for publication in *Journal of Physical Oceanography*. DOI 10.1175/JPO-D-19-0061.1.

Figure 6. Whitecap and wind stress retrieval of extreme wind cases of SMAP datasets (Y16 and M17) and comparison with models (9) and (10): (a) W_c, and (b) u_*; results obtained with both V and H polarizations are presented, statistics (b_0, b_1, b_2, and b_3) of comparing the modeled and retrieved W_c and u_* with both polarizations are printed at the lower right corners.

Figure 7. Whitecap and wind stress retrieval from SMOS dataset (R16) and comparison with models (9) and (10): (a) W_c, and (b) u_*; bin-averaged results obtained for θ=11°, 15°, 20°, …, 60°, and 64° are illustrated with various markers identified in the legend, un-averaged 35° results are shown with cyan dots in the background.

Figure 8. (a) Whitecap coverage dependence on wind speed, data are from observations tabulated in MTRXLS (Monahan 1971; Toba and Chaen 1973; Ross and Cardone 1974; Xu et al. 2000; Lafon et al. 2004, 2007; Sugihara et al. 2007) and C08 (Callaghan et al. 2008). Solid line is whitecap coverage model (9). (b) Whitecap coverage dependence on surface wave energy dissipation rate computed with wind and wave data reported in TLS (Toba and Chaen 1973; Lafon et al. 2004, 2007; Sugihara et al. 2007). Dashed line is linear function (11) given in H08 (Hwang and Sletten 2008). [Partially reproducing Figure 6 of Hwang and Sletten (2008)].

Figure 9. Whitecap and wind stress results combining from SFMR, SMAP, SMOS, and WindSat datasets discussed in this paper: (a) W_c, (b) u_*, and (c) energy dissipation rate E_t converted from whitecap coverage obtained by microwave radiometers and employing the linear relationship obtained by Hwang and Sletten (2008).

Figure A1. Determination of flat surface (specular) emissivity using data with U_{10}<2 m s^{-1}: (a, c) e_{0H}, and (b, d) e_{0V}. Superimposed black lines are fitted polynomial curves; red lines are analytical solutions computed with s=35 psu and T_s=290 K. Top and bottom rows show results for data used in

Accepted for publication in *Journal of Physical Oceanography*. DOI 10.1175/JPO-D-19-0061.1.

Figures 3 and 4, respectively.

Figure A2. WindSat $\Delta e_p(U_{10})$ of Figure 3 data (blue markers and light-colored dots for bin-averaged and un-averaged results, respectively), and comparison with M09 (red markers) and analytical solutions (black lines): (a) 10.7 GHz, (b) 18.7 GHz, (c) 23.7 GHz, and (d) 37.0 GHz. Mean and standard deviation of EIA are given in the second set of numbers inside parentheses at the upper left corner of each panel.

Accepted for publication in *Journal of Physical Oceanography*. DOI 10.1175/JPO-D-19-0061.1.

List of Table

Table 1. Lookup table (LUT) for retrieving W_c and u_* from WindSat 6.8 GHz Δe_H observations. Additional LUTs for SFMR, WindSat and L-band radiometers at selected incidence angles are given in the supplemental material.

(WindSat 6.8 GHz, θ=53.5°, *p*=H)

Columns: (1) U_{10} (m/s), (2) 100W_c, (3)100u_* (m/s), (4) 100Δe_p, (5) 100Δe_{pf}, (6) 100$\Delta e_{pf}/\Delta e_{ps}$

(1)	(2)	(3)	(4)	(5)	(6)
2.50	0.00	8.05	0.71	0.00	0.00
7.50	0.16	28.47	1.87	0.02	0.87
12.50	1.40	52.51	3.27	0.14	4.37
17.50	3.81	78.42	4.62	0.39	8.52
22.50	7.88	104.85	5.89	0.83	14.08
27.50	13.64	130.59	7.36	1.47	20.00
32.50	20.75	154.45	9.04	2.31	25.60
37.50	26.80	171.08	10.44	3.07	29.45
42.50	31.34	182.13	11.44	3.68	32.13
47.50	36.01	192.55	12.48	4.32	34.64
52.50	40.81	202.43	13.56	5.02	37.02
57.50	45.72	211.85	14.68	5.77	39.29
62.50	50.75	220.86	15.65	6.58	42.02
67.50	55.87	229.53	16.90	7.45	44.07
72.50	61.09	237.88	18.23	8.39	46.01
77.50	66.40	245.94	19.39	9.40	48.49
82.50	71.80	253.75	20.88	10.50	50.29
87.50	77.28	261.33	22.21	11.69	52.66
92.50	82.84	268.69	23.90	12.99	54.36
97.50	88.47	275.86	25.43	14.41	56.66

Accepted for publication in *Journal of Physical Oceanography*. DOI 10.1175/JPO-D-19-0061.1.

Table A1. Polynomial coefficients of WindSat flat surface (specular) emissivity: $e_{0p} = A_2 T_s^2 + A_1 T_s + A_0$.

Freq., Pol.	A_2	A_1	A_0
Jan 2014			
10.7 GHz, H	1.5120×10^{-5}	-8.9560×10^{-3}	1.5910
18.7 GHz, H	1.2115×10^{-5}	-7.8507×10^{-3}	1.5227
23.8 GHz, H	2.9801×10^{-5}	-1.8515×10^{-2}	3.1573
37.0 GHz, H	1.5549×10^{-5}	-1.1144×10^{-2}	2.2447
10.7 GHz, V	2.2762×10^{-5}	-1.3564×10^{-2}	2.5440
18.7 GHz, V	2.8351×10^{-5}	-1.7902×10^{-2}	3.4152
23.8 GHz, V	3.1341×10^{-5}	-2.0123×10^{-2}	3.8107
37.0 GHz, V	2.8410×10^{-5}	-1.9355×10^{-2}	3.8787
Jul 2014			
10.7 GHz, H	1.0219×10^{-5}	-6.1208×10^{-3}	1.1812
18.7 GHz, H	9.4038×10^{-6}	-6.3718×10^{-3}	1.3221
23.8 GHz, H	2.3373×10^{-5}	-1.4908×10^{-2}	2.6537
37.0 GHz, H	1.1402×10^{-5}	-8.8195×10^{-3}	1.9199
10.7 GHz, V	2.8709×10^{-5}	-1.6973×10^{-2}	3.0335
18.7 GHz, V	4.0179×10^{-5}	-2.4729×10^{-2}	4.3997
23.8 GHz, V	4.4857×10^{-5}	-2.7885×10^{-2}	4.9262
37.0 GHz, V	3.9726×10^{-5}	-2.5919×10^{-2}	4.8308

Accepted for publication in *Journal of Physical Oceanography*. DOI 10.1175/JPO-D-19-0061.1.

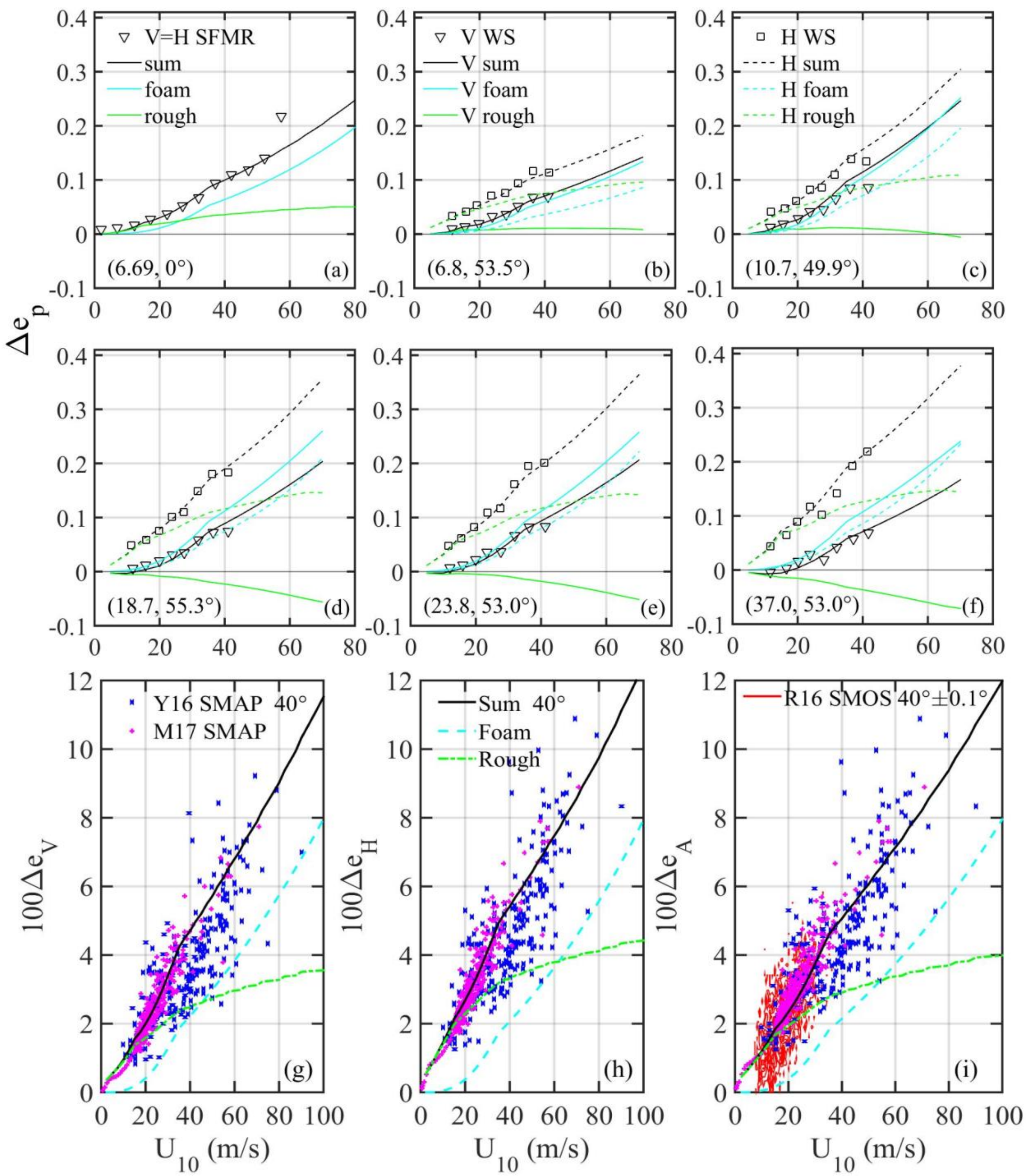

Figure 1. Calculated Δe_V and Δe_H at various microwave frequencies, and comparison with field data. Top two rows (M09 and S19, triangle for *V* and square for *H*): (a) 6.69 GHz, (b) 6.8 GHz, (c) 10.7 GHz, (d) 18.7 GHz, (e) 23.8 GHz, and (f) 37.0 GHz. Sum, foam and roughness contributions are given by black, cyan and green curves, solid and dashed lines show vertical and horizontal polarizations, respectively. The two numbers in parentheses are frequency (in GHz) and EIA. Bottom row (L band 1.41 GHz, θ=40°): (g) Δe_V, Y16 and M17 (SMAP), (h) Δe_H, Y16 and M17 (SMAP), and (i) Δe_A, Y16 and M17 (SMAP) and R16 θ=40°±0.1° (SMOS)..

Accepted for publication in *Journal of Physical Oceanography*. DOI 10.1175/JPO-D-19-0061.1.

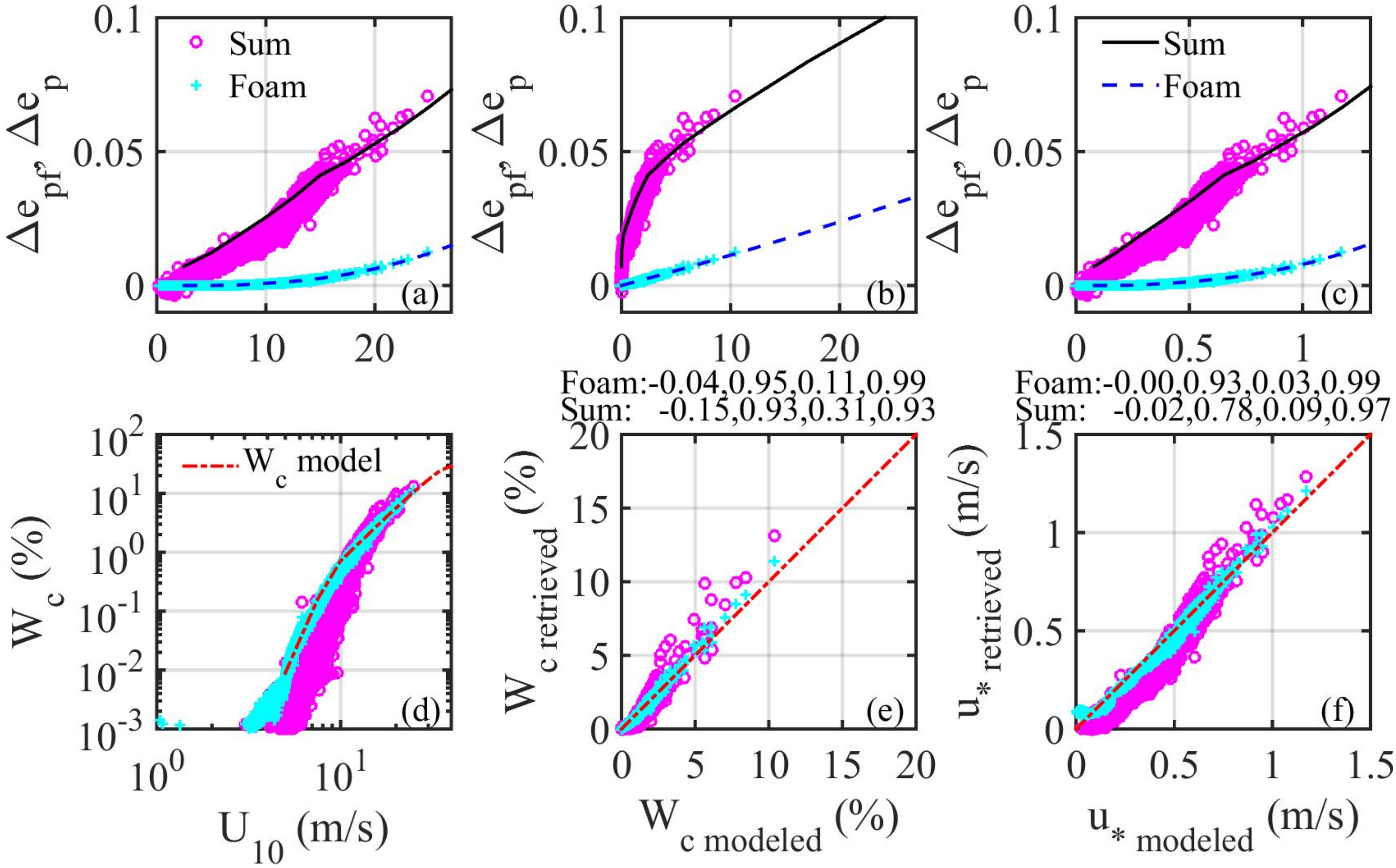

Figure 2. Illustration of whitecap and surface wind stress retrieval using Δe_p, WindSat 6.8 GHz horizontal polarization data are used for example ($p = H$): (a) $\Delta e_p(U_{10})$ and $\Delta e_{pf}(U_{10})$, (b) $\Delta e_p(W_c)$ and $\Delta e_{pf}(Wc)$, (c) $\Delta e_p(u_*)$ and $\Delta e_{pf}(u_*)$, (d) $W_c(U_{10})$ retrieved with Δe_p and Δe_{pf}, (e) comparison of modeled and retrieved W_c from Δe_p and Δe_{pf}, and (f) comparison of modeled and retrieved u_* from Δe_p and Δe_{pf}. In (e) and (f), statistics (b_0, b_1, b_2, and b_3) of modeled and retrieved W_c and u_* with Δe_p and Δe_{pf} are printed at the top.

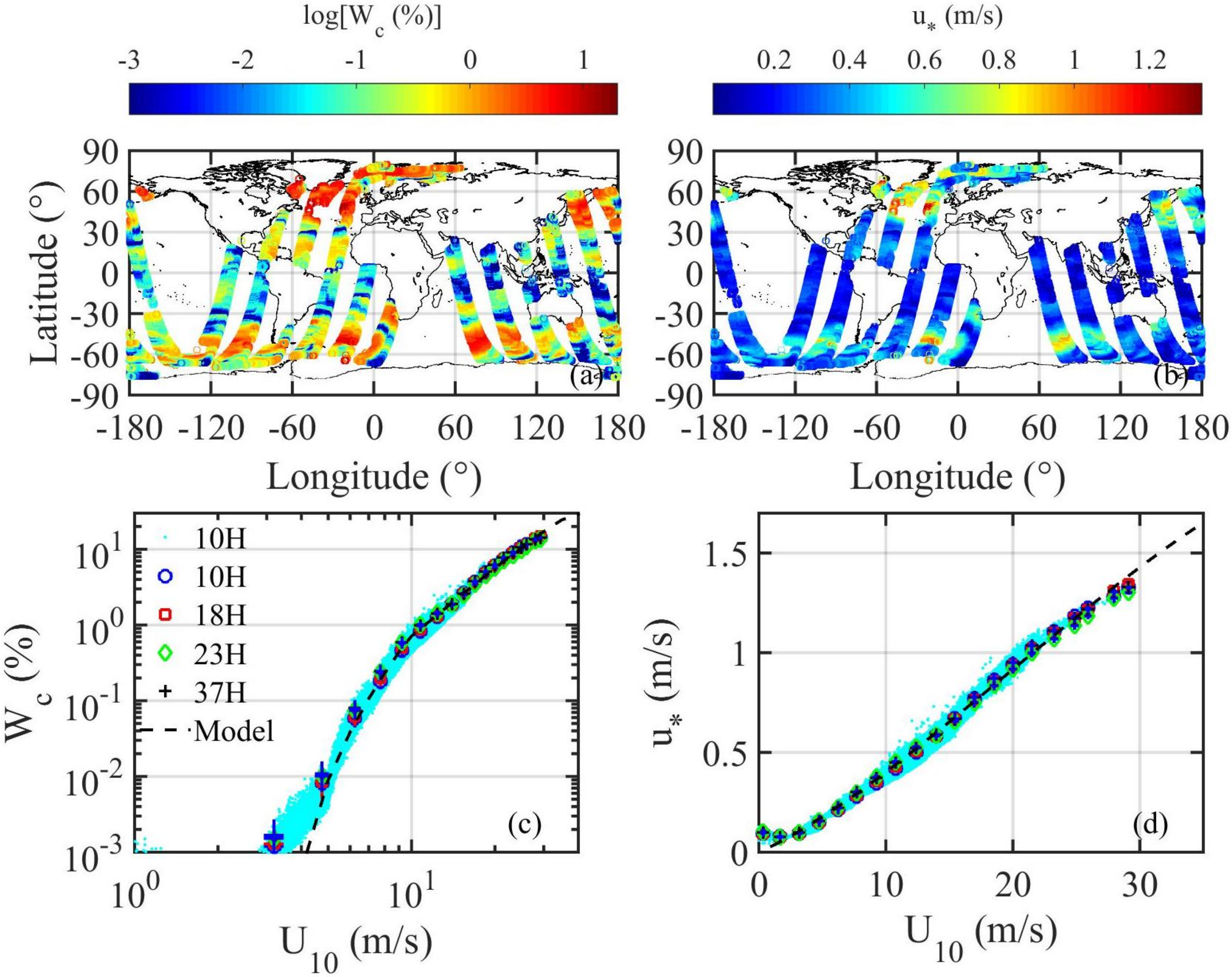

Figure 3. Snapshots (~10 h) of WindSat global retrieval of (a) W_c, and (b) u_* on 05 Jan 2014 (in northern winter). The dependence on wind speed is given in (c) for W_c, and (d) for u_*, bin-averaged results shown with colored markers are from four microwave frequencies identified in the legend; un-averaged results for 10.7 GHz are superimposed with cyan dots in the background..

Accepted for publication in *Journal of Physical Oceanography*. DOI 10.1175/JPO-D-19-0061.1.

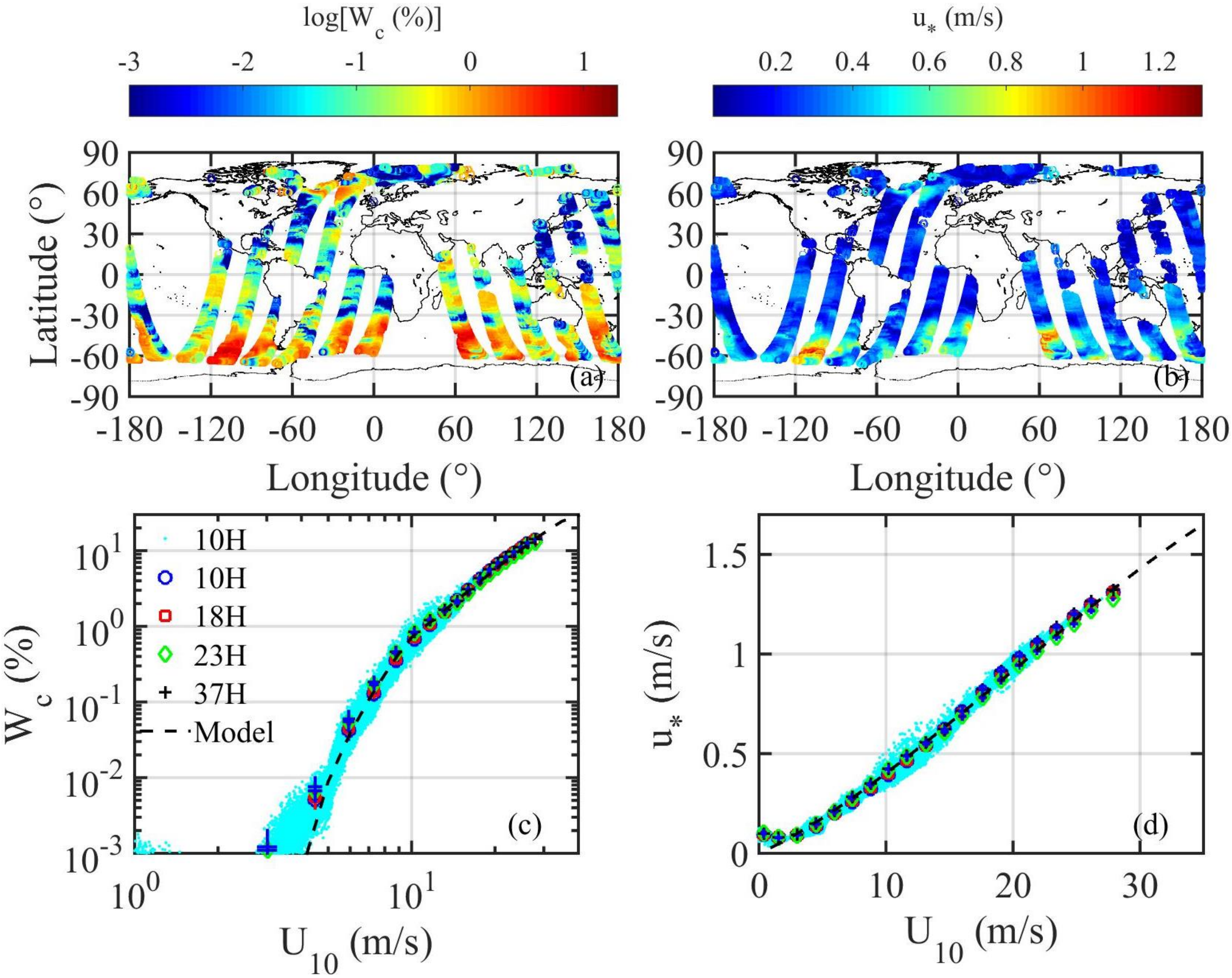

Figure 4. As Figure 3 but on 01 Jul 2014 (in southern winter).

Accepted for publication in *Journal of Physical Oceanography*. DOI 10.1175/JPO-D-19-0061.1.

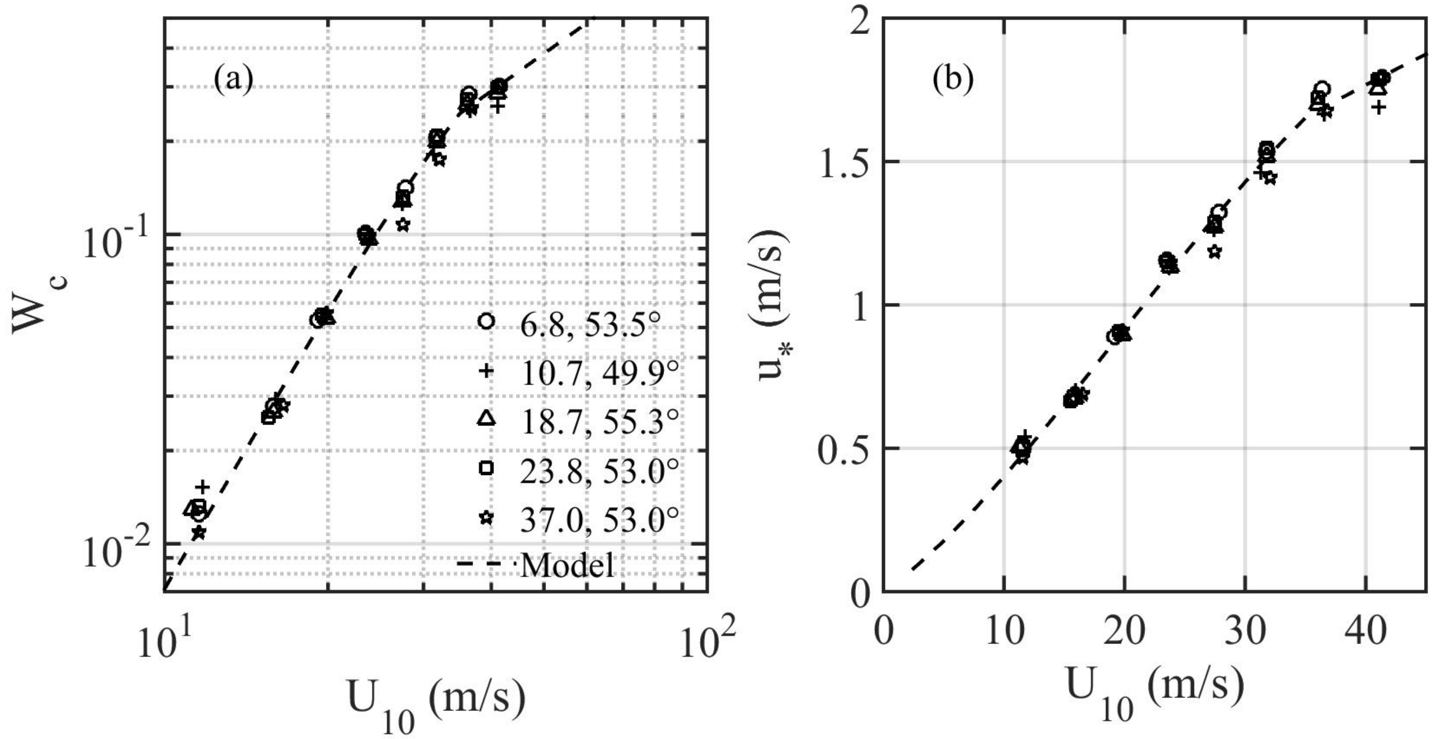

Figure 5. Whitecap and wind stress retrieval from five frequencies of M09 WindSat dataset and comparison with models (9) and (10): (a) W_c, and (b) u_*.

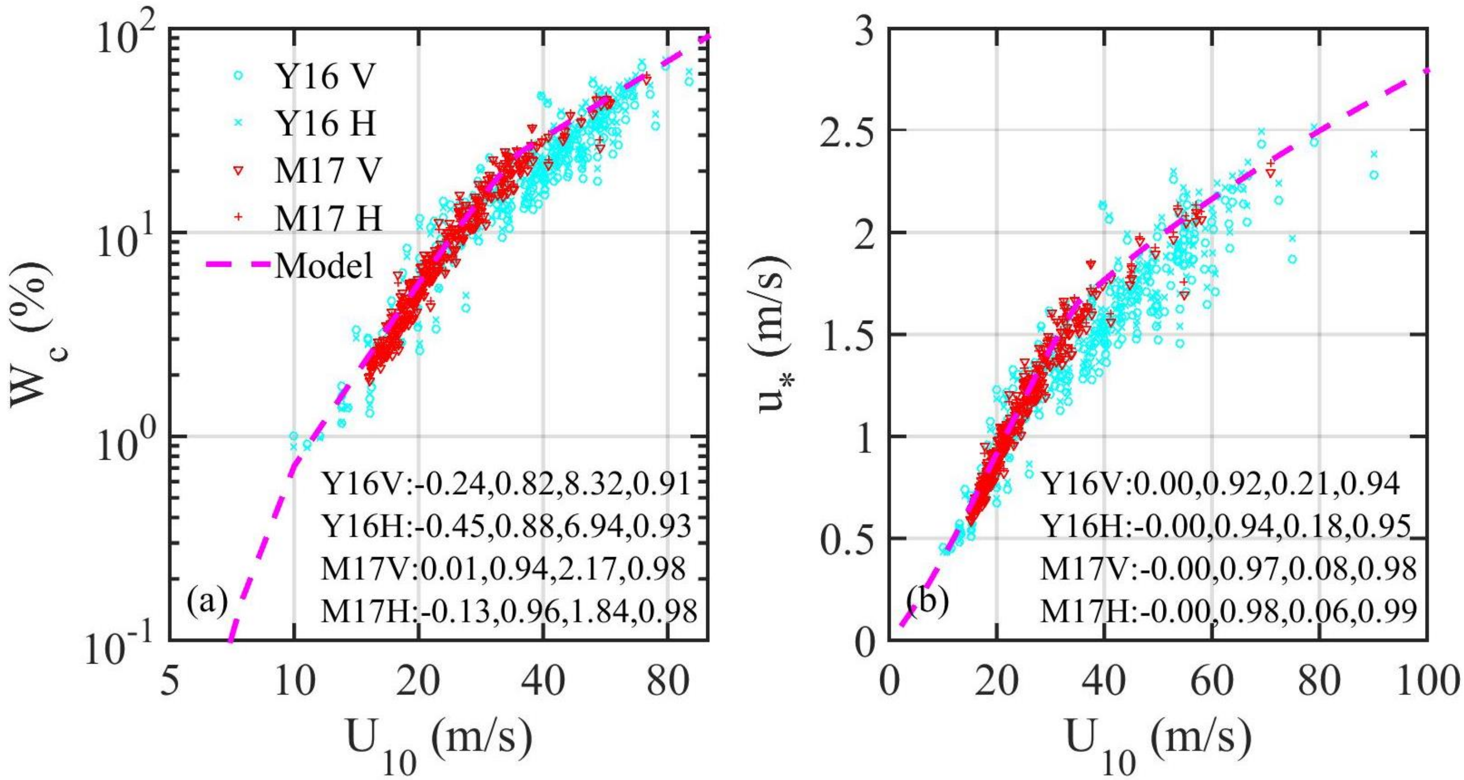

Figure 6. Whitecap and wind stress retrieval of extreme wind cases of SMAP datasets (Y16 and M17) and comparison with models (9) and (10): (a) W_c, and (b) u_*; results obtained with both V and H polarizations are presented, statistics (b_0, b_1, b_2, and b_3) of comparing the modeled and retrieved W_c and u_* with both polarizations are printed at the lower right corners.

Accepted for publication in *Journal of Physical Oceanography*. DOI 10.1175/JPO-D-19-0061.1.

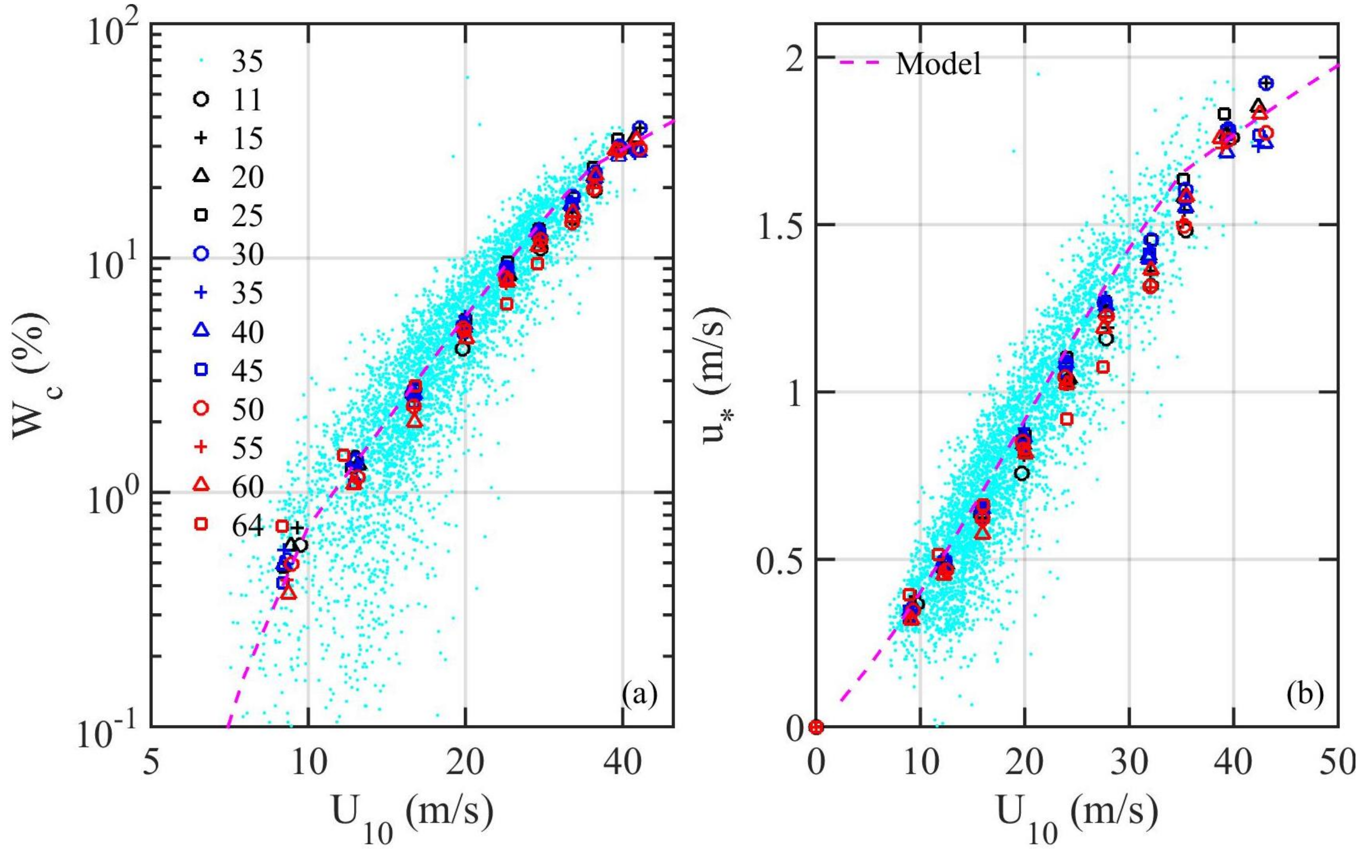

Figure 7. Whitecap and wind stress retrieval from SMOS dataset (R16) and comparison with models (9) and (10): (a) W_c, and (b) u_*; bin-averaged results obtained for θ=11°, 15°, 20°, …, 60°, and 64° are illustrated with various markers identified in the legend, un-averaged 35° results are shown with cyan dots in the background.

Accepted for publication in *Journal of Physical Oceanography*. DOI 10.1175/JPO-D-19-0061.1.

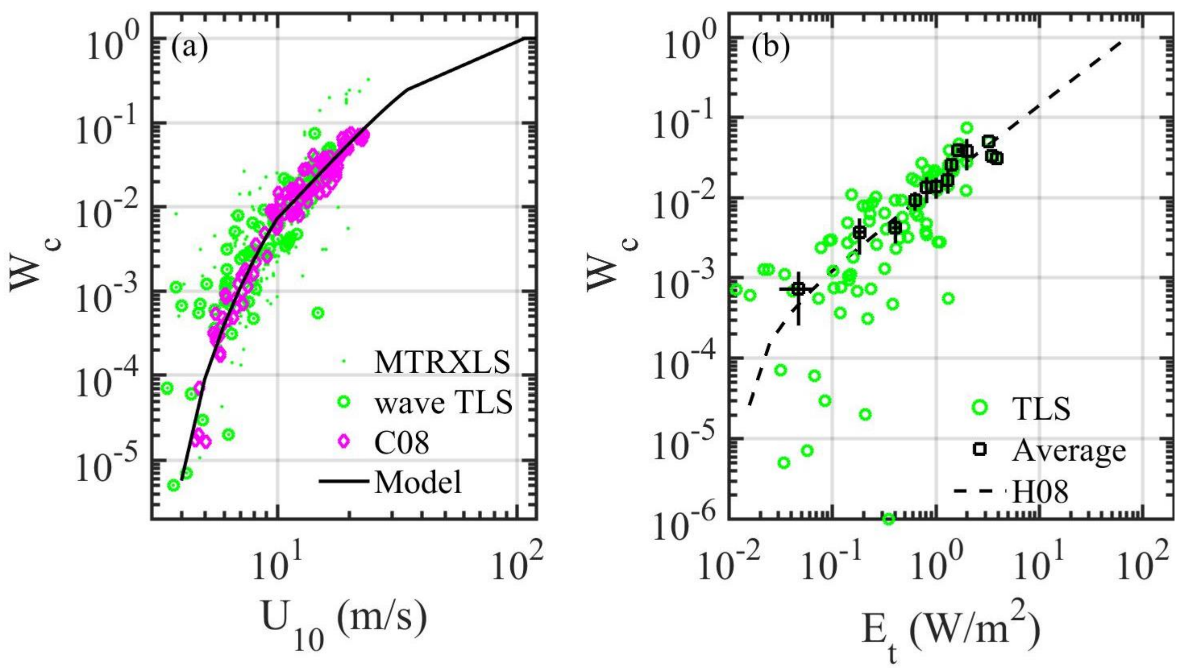

Figure 8. (a) Whitecap coverage dependence on wind speed, data are from observations tabulated in MTRXLS (Monahan 1971; Toba and Chaen 1973; Ross and Cardone 1974; Xu et al. 2000; Lafon et al. 2004, 2007; Sugihara et al. 2007) and C08 (Callaghan et al. 2008). Solid line is whitecap coverage model (9). (b) Whitecap coverage dependence on surface wave energy dissipation rate computed with wind and wave data reported in TLS (Toba and Chaen 1973; Lafon et al. 2004, 2007; Sugihara et al. 2007). Dashed line is linear function (11) given in H08 (Hwang and Sletten 2008). [Partially reproducing Figure 6 of Hwang and Sletten (2008)].

Accepted for publication in *Journal of Physical Oceanography*. DOI 10.1175/JPO-D-19-0061.1.

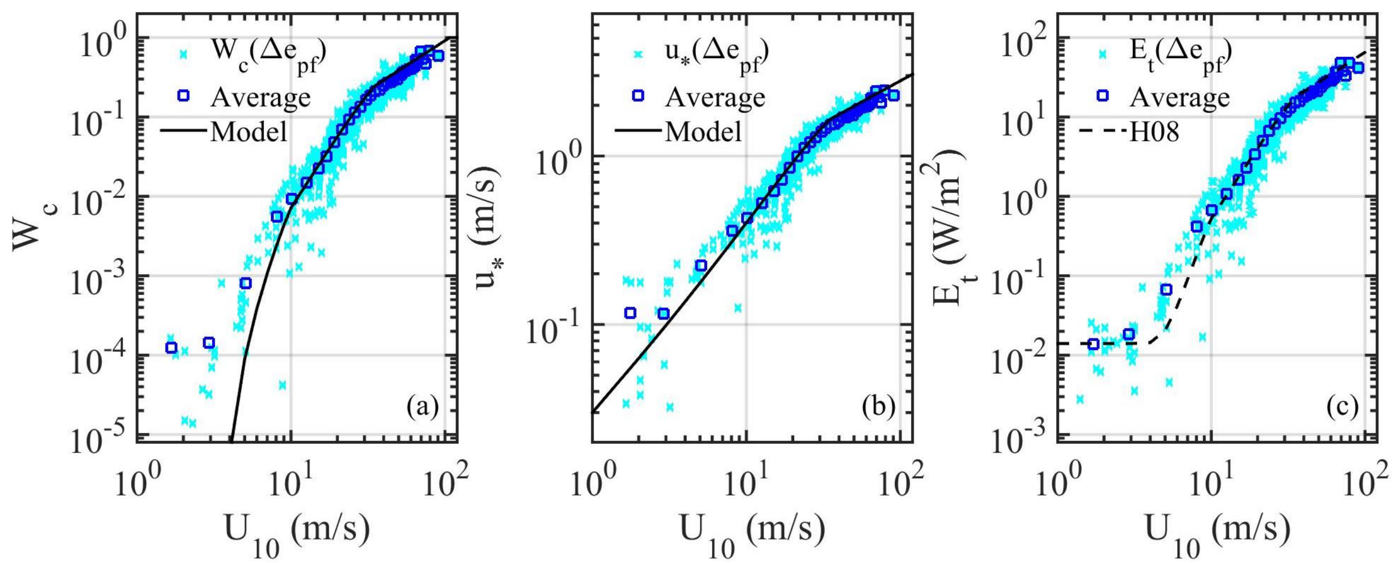

Figure 9. Whitecap and wind stress results combining from SFMR, SMAP, SMOS, and WindSat datasets discussed in this paper: (a) W_c, (b) u_*, and (c) energy dissipation rate E_t converted from whitecap coverage obtained by microwave radiometers and employing the linear relationship obtained by Hwang and Sletten (2008).

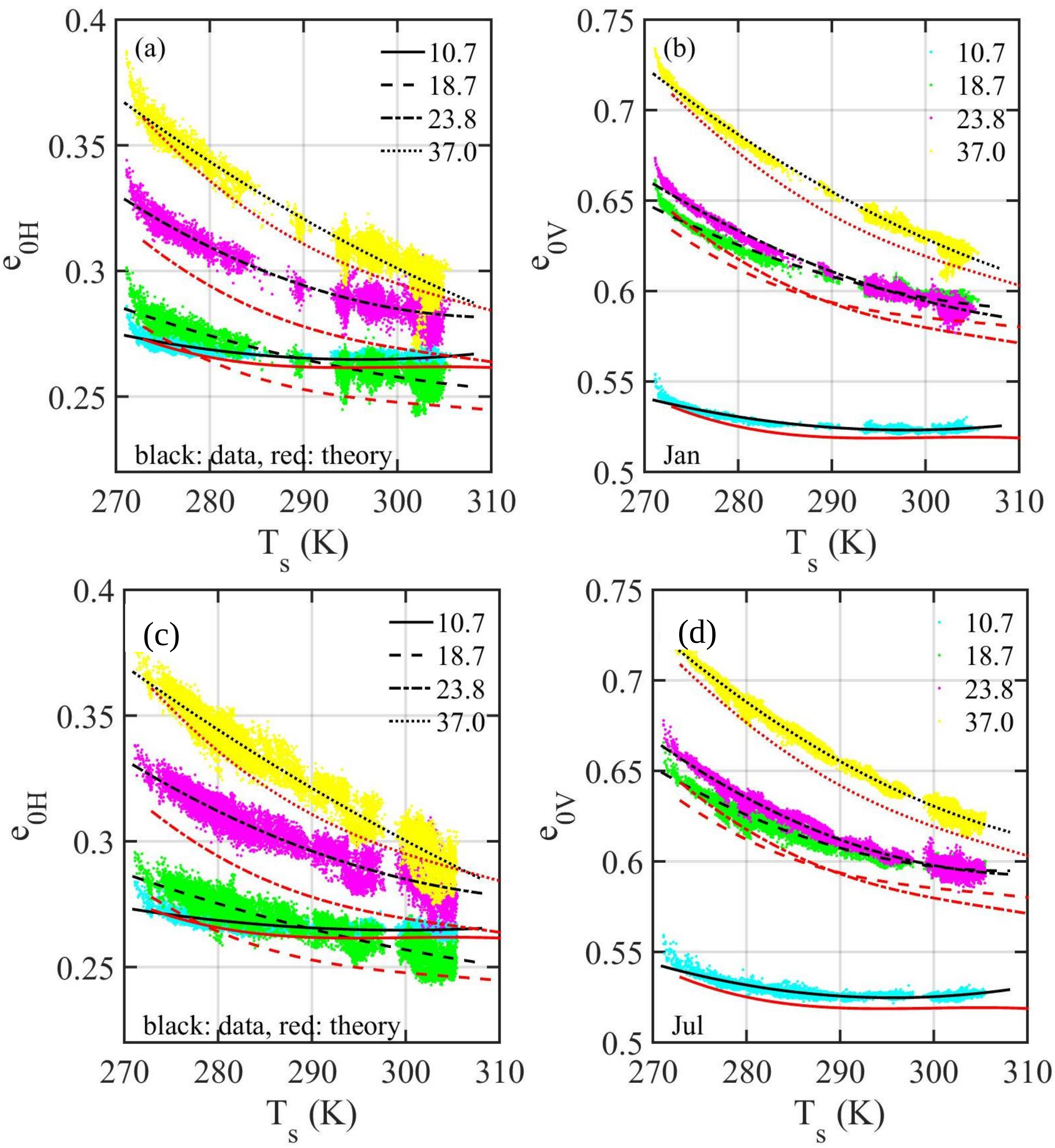

Figure A1. Determination of flat surface (specular) emissivity using data with U_{10}<2 m s^{-1}: (a, c) e_{0H}, and (b, d) e_{0V}. Superimposed black lines are fitted polynomial curves; red lines are analytical solutions computed with s=35 psu and T_s=290 K. Top and bottom rows show results for data used in Figures 3 and 4, respectively.

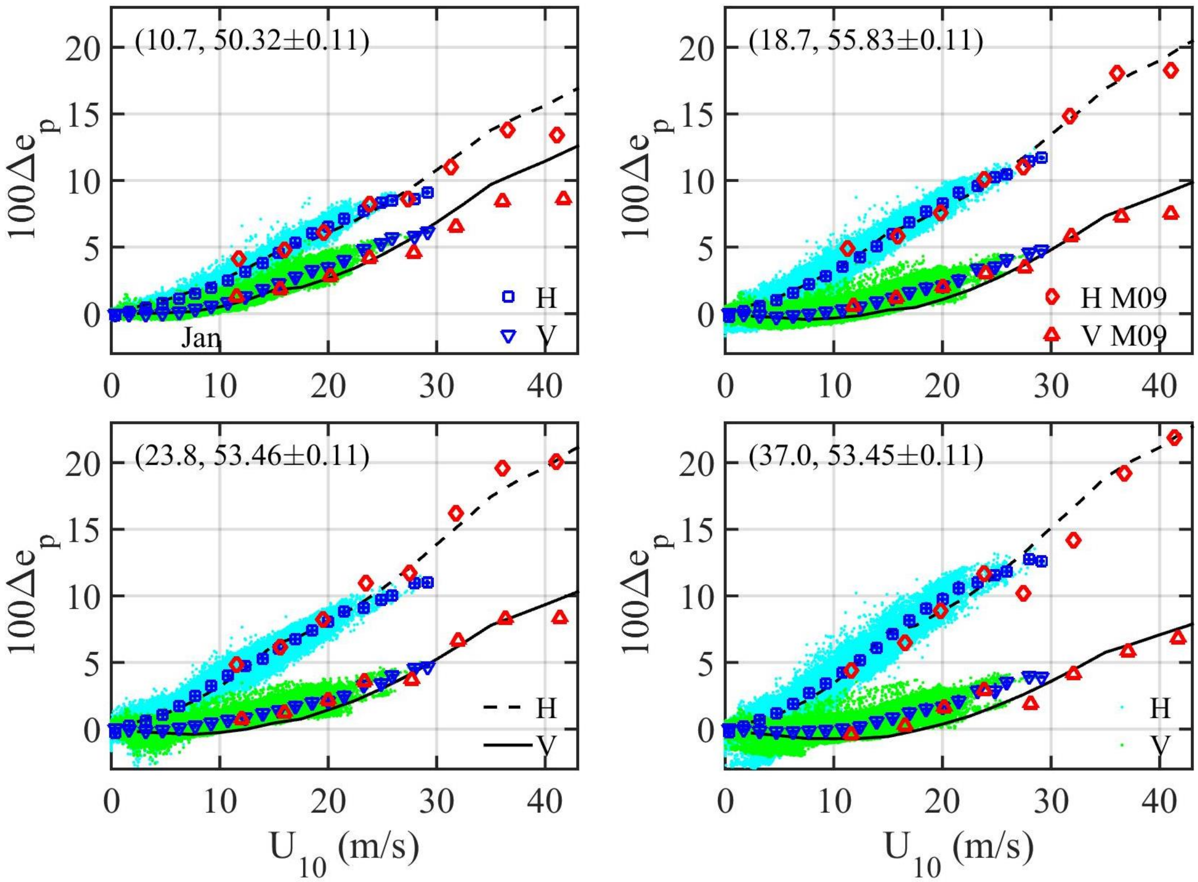

Figure A2. WindSat $\Delta e_p(U_{10})$ of Figure 3 data (blue markers and light-colored dots for bin-averaged and un-averaged results, respectively), and comparison with M09 (red markers) and analytical solutions (black lines): (a) 10.7 GHz, (b) 18.7 GHz, (c) 23.7 GHz, and (d) 37.0 GHz. Mean and standard deviation of EIA are given in the second set of numbers inside parentheses at the upper left corner of each panel.